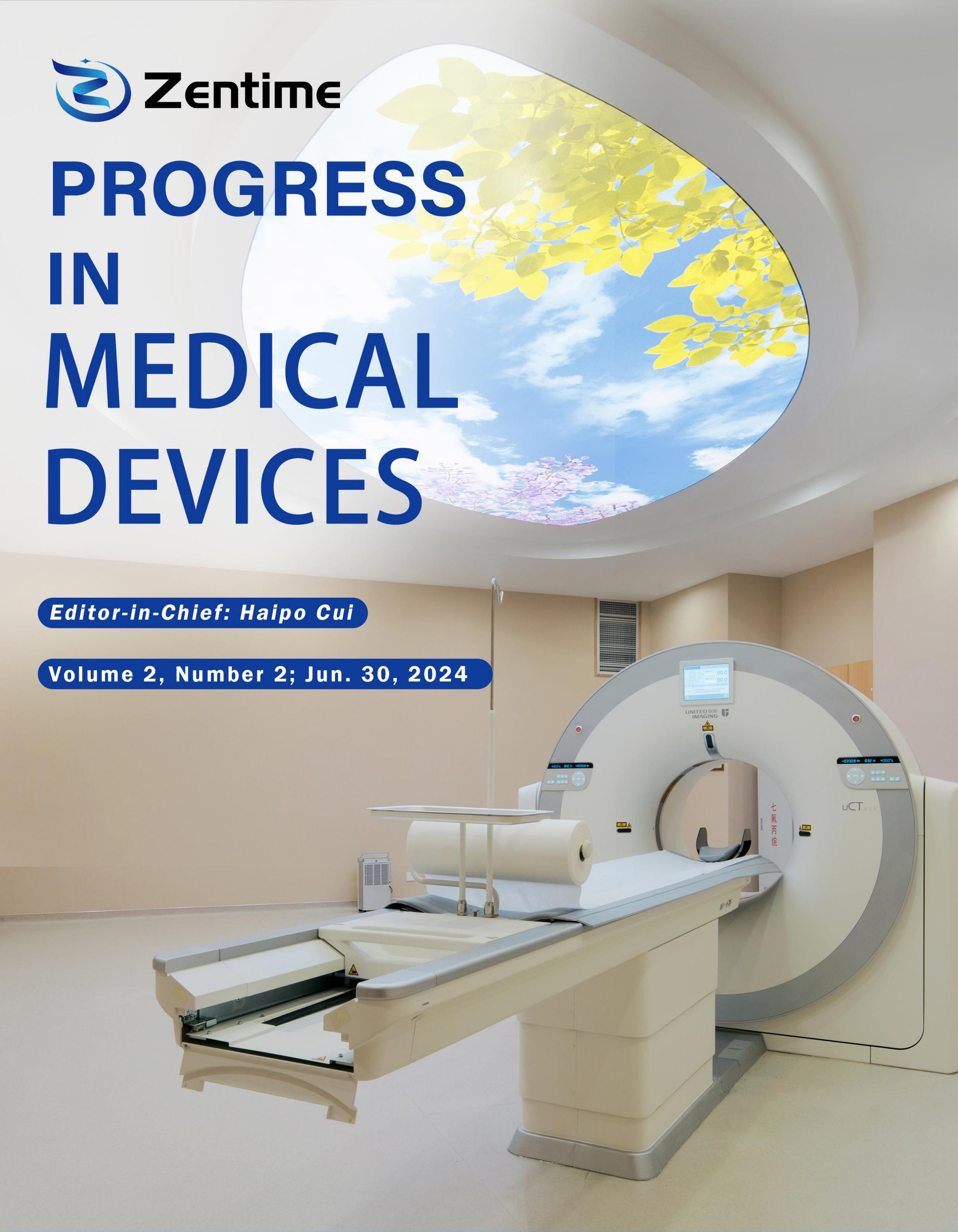

Zentime

# PROGRESS IN MEDICAL DEVICES

Editor-in-Chief: Haipo Cui

Volume 2, Number 2; Jun. 30, 2024

ISSN: 2957-5478

Published by ZENTIME PUBLISHING CORPORATION

Progress in Medical Devices
eISSN: 2957-5478

Review Article https://doi.org/10.61189/585036wxisob

# Research progress and clinical application of cooled radiofrequency ablation

Dandan Gu, Ruiyan Qian, Danni Rui, Difang Liu, Haitao Yao, Yifan Yang, Yu Zhou

School of Health Sciences and Engineering, University of Shanghai for Science and Technology, Shanghai 200093, China.

**Corresponding author:** Yu Zhou.

**Declaration of conflict of interest:** None.

Received December 4, 2023; Accepted January 8, 2024; Published June 30, 2024

## Highlights

- Cooled radiofrequency ablation (CRFA) represents an advancement in RF ablation, enhancing treatment safety and efficacy through electrode cooling.
- CRFA principles, electrode cooling methods, efficacy evaluation, and an overview of major CRFA devices available on the market are comprehensively analyzed.
- The clinical advancements in applying CRFA technology indicate its feasibility and safety as a viable treatment modality.

## Abstract

Radiofrequency ablation (RFA) is a minimally invasive clinical treatment that uses radiofrequency energy to generate heat, resulting in the thermal necrosis of targeted tissues. To enhance the therapeutic benefits of traditional RFA, cooled RFA (CRFA) technology has been developed. CRFA incorporates cooling technology to prevent thermal damage and rapid impedance changes caused by tissue overheating. This review article provides a comprehensive overview of various types of cooling electrode needles used in CRFA, as well as an evaluation of their efficacy and clinical applications. We discuss the advantages of CRFA, including its minimally invasive nature, improved safety profile, and highly effective treatment outcomes. Nevertheless, certain problems and limitations are also addressed to optimize the potential of CRFA as a clinical treatment option. Overall, CRFA has promising prospects. With continued advancements in technology and further research, this innovative treatment modality is expected to significantly impact the treatment of a wide range of medical conditions.

**Keywords**: Cooled radiofrequency ablation, cooling electrode needle, therapeutic effect evaluation, clinical application

## Introduction

Tumor ablation techniques encompass a wide range of methods, including chemical ablation, thermal ablation, irreversible electroporation, and high-intensity focused ultrasound [1].

Chemical ablation, a non-energy-based technique, achieves ablation by injecting ethanol and acetic acid into the tumor, causing coagulative necrosis [2].

Thermal ablation is further divided into radiofrequency ablation (RFA), microwave ablation, cryoablation, and laser ablation. Microwave ablation involves precise insertion of a microwave antenna into the tumor center under visual guidance. The non-insulated tip of the microwave antenna emits electromagnetic waves at frequencies of 915 or 2,450 MHz directly to the tumor tissue, where water molecules intensively collide [3]. This process leads to rapid heating and coagulative necrosis of tumor cells. RFA, recognized for its safety and effectiveness, utilizes radiofrequency energy between 375-500 KHz to heat and destroy diseased tissue and is increasingly used across various clinical settings [4].

Cryoablation employs argon-helium technology, guided by the Joule-Thomson effect, alternating high-pressure argon gas to freeze the tumor

**Address correspondence to: Yu Zhou**, School of Health Sciences and Engineering, University of Shanghai for Science and Technology, No.516 Jungong Road, Shanghai 200093, China. Tel: 18021042556. E-mail: zhouyu@usst.edu.cn.

**Table 1. The advantages and disadvantages of different ablation techniques**

| Ablation technique | The advantages | The disadvantages |
|---|---|---|
| Thermal ablation | Cheap<br>Quick and easy<br>Well tolerated | Chemical drugs are not evenly distributed<br>Multiple recurrences<br>Requires multiple treatments |
| Radiofrequency ablation | Cheap<br>Various electrode shapes<br>The most widely studied and available | The ablation zone is not visible during ablation<br>Thermal sedimentation effect<br>Finite ablation zone |
| Microwave ablation | High temperature<br>Large ablation area<br>Short ablation time | General anesthesia<br>More difficult than radiofrequency ablation<br>Easily damage healthy organs and tissues |
| Cryoablation | The ablation zone is visible during ablation<br>Reduce pain | Long ablation time<br>High risk of bleeding<br>The possibility of hypothermia shock |
| Laser ablation | Precise positioning, suitable for high-risk locations<br>Reduce image artifacts | Small ablation area<br>Limited energy penetration |
| Irreversible electroporation | Short ablation time<br>Retain adjacent organizational structures<br>Clearly define the ablation zone | General anesthesia<br>The single ablation volume is small |
| High-intensity focused ultrasound | Non-invasive, in vitro | The patient needs to be still<br>Long treatment time |

to -140 °C and helium to rapidly reheat it to 40 °C. This freeze-thaw cycle causes protein denaturation, cellular dehydration, membrane rupture, and thrombosis in microvessels, culminating in the destruction of tumor cells [5-7].

Irreversible electroporation, an innovative ablation technique, uses high-voltage, low-energy direct currents to create nanoscale pores on the cell membrane, disrupting cellular homeostasis and inducing apoptosis [8].

High-intensity focused ultrasound takes advantage of the unique characteristics of sound waves with frequencies between 0.8 and 3.5 MHz. These sound waves are enhanced and focused on a specific distance from the transducer. By using sound energy (up to 10,000 W/cm$^2$), intense tissue movement is induced, generating heat and causing necrosis at the target location [9].

Cooled RFA (CRFA) offers comparable safety to traditional RFA [10]. It improves treatment outcomes by incorporating cooling functionality to the electrode needle based on RFA technology. This innovative approach has found widespread application in various clinical settings. This review aims to outline the research progress and clinical applications of CRFA. **Table 1** shows the advantages and disadvantages of different ablation techniques.

**The principle of CRFA**

The treatment mechanisms of CRFA and RFA share a common foundation, employing thermal effects for the ablation of pathological tissues. A closed circuit is formed between the ablation device and the target tissue during the ablation process. As the alternating current flows through the tissue, rapid fluctuations in the electromagnetic field cause polar water molecules within the tissue to oscillate at high speeds. This motion generates heat that triggers the evaporation, drying, shrinkage, and shedding of water within and surrounding the cells, ultimately resulting in sterile necrosis and achieving the desired therapeutic effect [11].

In monopolar ablation, the circuit current flows between the electrode needle and the negative plate; while in bipolar ablation, the circuit current flows back and forth between the two electrode needles, which act as the anode and cathode of the ablation [12]. In multistage ablation, multiple bipolar applicators are used in conjunction to enhance thermal effect and create a larger spherical coagulation zone [13].

The energy generator of the ablation device produces high frequency alternating current. As the current changes, the ions within the tissue interact and produce heat, which raises the temperature of the lesion tissue to above 60

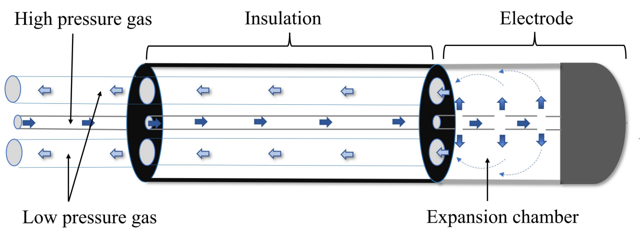


**Figure 1. Schematic diagram of air-cooled electrode needle.**

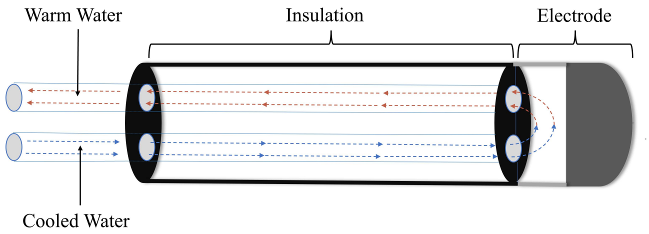


**Figure 2. Schematic diagram of liquid-cooled electrode needle.**

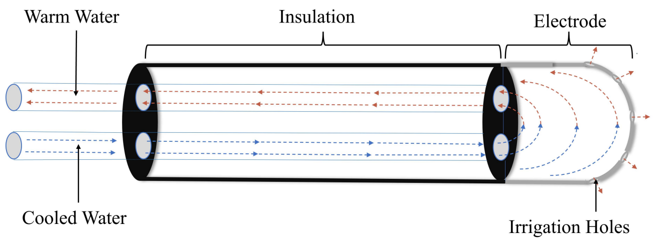


**Figure 3. Schematic diagram of the cold and wet electrode needle.**

°C, inflicting irreversible tissue damage [14]. However, traditional RFA has a crucial limitation. Tissue in contact with the electrode needle is prone to excessive heat and carbonization, leading to thrombus formation, eschar, and carbonization on the electrode surface. This can affect energy output and ablation efficacy. To address these issues, cold pole RFA system was developed to improve ablation efficiency and surgical success rates. CRFA lowers the temperature of tissues near the radiofrequency electrode, reduces the surrounding tissue carbonization, and achieves a larger necrotic area [15].

## Types of electrodes in CRFA and their efficacy evaluation

### *Types of cooling electrode needles*

Based on the cooling method, cooling electrode needles can be divided into internally and externally cooled electrode needles. Internally cooled electrode needles utilize gas or liquid within the device to dissipate thermal energy from the electrode needle through heat transfer, thereby achieving the desired cooling effect. Hence, internal cooling electrode needles encompass both gas-cooled and liquid-cooled electrode needles. In contrast, externally cooled electrode needles exclusively employ cooling liquid as the cooling medium, inheriting the advantages of interior cooling electrode needles while incorporating flushing holes around the electrode.

The air-cooled electrode needle RF system utilizes pressurized $CO_2$, $N_2$, or CO as a cooling medium, which is released through a standard gas cylinder, pressure tube, switch, and pressure regulator. As shown in **Figure 1**, the gas flows through a nozzle in the electrode needle into the expansion chamber, where the Joule-Thompson principle produces a cooling effect to cool the electrode needle [16, 17]. Early studies have shown promising results for air-cooled RFA. Carrara et al. used this technique to ablate the liver and spleen of pigs, followed by pathological and histological analysis of each ablation, confirming its feasibility and safety [18]. Similarly, Rempp et al. demonstrated that cryogenic air-cooled radiofrequency electrodes produced a more extensive ablation range and lowered ellipse index than conventional RFA in ex vivo bovine liver; they also observed that increasing power with stable air pressure and standardized application time increased the short axis of the ablation range [19]. Further, Hoffmann et al. used air-cooled ablation electrodes in ex vivo bovine liver and found that impedance-controlled ablation resulted in a maximum short axis diameter of 51.1mm for the ablation zone [20]. These results indicate the potential of air-cooled electrode needle RF systems in ablation and pave the way for further studies to explore its safety and efficacy.

As illustrated in **Figure 2**, the liquid-cooled electrode needle ablation system utilizes an internal tube to circulate cold saline or chilled water into the electrode needle via a perfusion pump. This type of electrode needle, exemplified by the Valleylab electrode needle, is widely used in clinical practice, where cooling fluid remains isolated from both the bloodstream and the tissue targeted for ablation. The system expels the heated effluent through an outflow tube to an external collection unit, effectively cooling the electrode tip internally and moderating the temperature of both the electrode tip and adjacent tissue [21]. The liquid-cooled electrode ablation covers a larger area than conventional

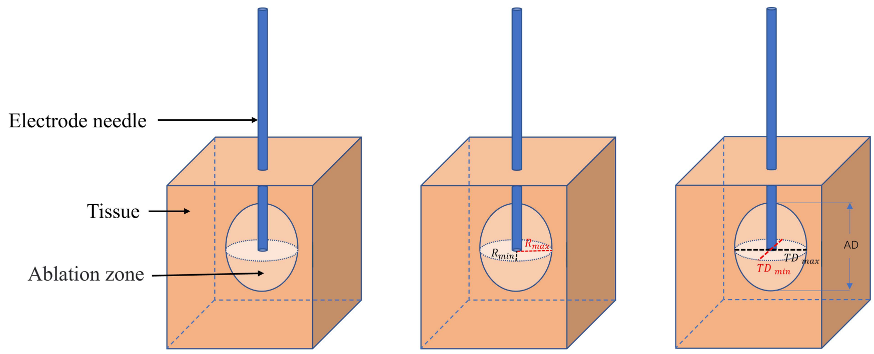


**Figure 4. Schematic diagram of ablation evaluation.** TD, transverse diameter.

RFA, offering a simple, cost-effective method for producing larger, more spherical lesions [22-23]. Solbiati et al. used internal cooling electrodes in 22 patients who were followed for at least five years, and demonstrated that using an optimized algorithm with a single internally cooled electrode to deliver RF energy to liver tumors produced a more significant, relatively spherical, and reproducible necrotic volume with more prolonged electrode tip exposure [24]. This approach can reduce ablation duration and increase ablation size with minimal adverse event rates. Yu et al. used an internally cooled directional electrode for ablation, producing a hemispherical ablation area that minimized thermal damage to adjacent organs by not extending beyond the hemisphere opposite the needle insertion site [25].

The efficacy of ablation using an external cold-cooled electrode needle (also known as a cold-wet electrode) has also been well-documented. **Figure 3** illustrates the technique, which incorporates a cooling electrode and a hole for cold saline rinsing, directly flushing the electrode tip and the surrounding tissue. The initial cold-wet electrode contained two coaxial cavities and a single saline channel, delivering coolant at a rate of at 40 ml/min and saline at 1 ml/min. This design improved the electrical and thermal conductivity of the tissue, significantly enhancing radiofrequency energy transmission and expanding the damage range [26]. Later improvements to the wet electrode design introduced a single cavity with two micropores at its tip. Additionally, the infusion rates for both coolant and saline were increased to 100-120 ml/min and 1-1.2 ml/min, respectively, creating a broader and more circular ablation area than the closed internal cold electrode, thus further enhancing the procedure precision [27, 28]. Cha et al. conducted an ex vivo study comparing double cold and wet electrodes with double internal cold electrodes, finding that double cold and wet electrodes created more spheres and larger ablation areas [29]. It is critical, however, for physicians to ensure that saline is precisely applied within the designated treatment area to prevent the spread of current and reduce potential complications [30].

### *CRFA therapeutic effect evaluation*

Utilizing the cooled electrode probe in CRFA technology enables the maintenance of low temperatures over extended periods, ultimately resulting in a more expansive and evenly distributed ablation area. When being applied to tumor ablation in liver, kidney, heart, prostate, and other organs, CRFA ensures complete and homogeneous cell destruction. This is evident by a white tissue appearance after lesion cauterization, in contrast to the surrounding healthy tissue that appear darker red [31].

As depicted in **Figure 4**, the ablation range typically exhibits shapes like circular, elliptical, and conical. The ellipticity index (EI) is calculated using the formula EI=2AD/( $TD_{max}$ + $TD_{min}$ ), and the regularity index (RI) is determined by RI= $R_{min}/R_{max}$ . For an ideal ellipse, the ablation volume can be expressed as $\frac{\pi}{6} * AD * TD_{max} * TD_{min}$ (AD and TD refer to axial diameter and transverse diameter). Here, the maximum transverse diameter $TD_{max}$ refers to the maximum distance between two opposite edges of the re-assembled coagulation zone in the transverse plane. The minimum transverse diameter $TD_{min}$ represents the minimum distance between two opposite edges of the coagulation zone in the transverse plane, measured in millimeters [32]. These measurements are taken at the midpoint, intersecting the line of the maximum transverse diameter. The AD is defined as the distance between the proximal and distal edges of the clotting region on the axis of the electrode. The maximum radius $R_{max}$ denotes the maximum distance between the electrode axis and the edges of the coagulation zone in the transverse plane. The minimum radius $R_{min}$ is the minimum distance between the electrode axis and the edge of the solidification zone in the transverse plane [16, 19, 22, 25, 33]. In *ex vivo* bovine liver, Clasen et al. conducted multipolar RFA and determined the relationship between coagulation volume and applied energy using nonlinear regression analysis, yielding a linear function V=0.61E+40.7 (r^2 = 0.87) for calculating coagulation volume [34].

## Several major CRFA equipment on the domestic and foreign markets

Presently, RFA stands as the prevalent ablative technique in the market, whereas CRFA, despite its later emergence, currently holds a smaller market share. Nevertheless, CRFA exhibits advantages such as reduced patient pain and fewer complications during the treatment process, rendering it a promising avenue for future growth. The cooling electrode needles, composed of a needle tip, handle, catheter, and connector, serve as a fundamental component of CRFA surgical equipment. Globally, major suppliers of CRFA needles include Boston Scientific and Medtronic from the United States, AtriCure from the United States, HealthTronics from the United States, Erbe from Germany, and IceCure Medical from Israel. Within China, suppliers like HYGEA and Surgnova are gaining recognition.

The COOLIEF* Cooling Radiofrequency System (Avanos Medical, Alpharetta, America) is a minimally invasive therapeutic ablation system specifically designed to target neural pain signals. It comprises an 80W radiofrequency generator, peristaltic pump, and treatment cable that capable of creating large-volume spherical ablation areas within nerve and intervertebral disc tissues without increasing the risk of adjacent tissue damage. While heating neural tissue, the system circulates water through the device, flowing through the tip of the RFA probe to keep it at a lower temperature, creating a larger treatment area compared to traditional RFA therapies [35]. This unique patented water-cooling technology has broadened the scope of radiofrequency treatments for chronic spinal, knee, and hip joint pain, contributing to an improved quality of life for patients.

The OSTEOCOOL™ Radiofrequency Ablation System (Boston Scientific, Marlborough, America) is a coaxial bipolar RFA device with a cooling apparatus in its radiofrequency tip. The radiofrequency device operates at a frequency of 468 KHz with a maximum output power of 50W. In a preclinical evaluation experiment on pig cervical spines, Pezeshki et al. utilized this system and demonstrated its capability to achieve large and reproducible ablation zones [36]. Importantly, the system effectively confined the ablation area within the vertebrae, without causing damage to nearby tissues or the spinal cord.

The Cool-tip™ Radiofrequency Ablation System E-Series (Medtronic, Dublin, America) is an internally cooled thermal ablation system designed for soft tissue tumors. The E-Series offers enhanced needle design and increased energy delivery. In comparison to other RFA systems, it can create a larger ablation area in a shorter time frame. This device enables real-time monitoring of temperatures near the ablation zone. Zhang et al. conducted a series of studies using this equipment on pig liver tissue, demonstrating that temperature monitoring in the ablation area is crucial for increasing the size of the coagulation zone [37].

The Dophi™ R150E Radiofrequency Ablation System (Surgnova, Beijing, China) can achieve both individual and simultaneous ablations with three needles. The system, equipped with a Swiss Watson Marlow water-cooling pump internally, reduces carbonization, ensuring efficient energy transmission, maximizes the ablation area, and concurrently minimizes thermal damage. This feature enhances the protection of surrounding neurovascular tissues, showcasing the system's capacity to balance effective energy delivery and tissue preservation.

The rapid development of CRFA, noted for its minimal thermal damage and effective tumor destruction, has led to a diverse range of devices now available on the market. **Table 2** presents several commonly used CRFA devices in the markets worldwide.

## Progress in the clinical application of CRFA

CRFA is a well-established modality for the treatment of liver cancer. Multipolar RFA, commonly used for small to medium-sized liver cancers, can sometimes result in overheating, leading to carbonation and rapid impedance rise. In contrast, traditional monopolar RFA requires overlapping techniques to achieve a sufficient ablation margin. Still, microbubbles during RFA can make it challenging to reposition the electrode accurately, leading to incomplete tumor ablation and higher recurrence risk [38]. Rhim et al. demonstrated the feasibility, safety, and efficacy of ultrasound-guided percutaneous RF ablation combined with artificial ascites for treating hepatocellular carcinoma (HCC) in the hepatic dome, with promising results over a 281.4-day follow-up period [39]. Tang et al. reported high complete ablation rates for liver tumors of varying sizes using ultrasound-guided cold needle RFA under local anesthesia, with low complication rates [40]. Clasen et al. further explored the use of MRI to guide the placement of a cooling electrode for treating HCC, achieving a high success rate with minimal complications, underscoring the

**Table 2. Several commonly used cooled radiofrequency ablation devices**

| Company | Cooled radiofrequency ablation equipment | Type of cooling | Electrode needle |
|---|---|---|---|
| Avanos Medical | COOLIEF Radiofrequency system | Liquid-cooled closed-loop internal cooling | Bipolar |
| Baylis Medical Company | OSTEOCOOL™ Radiofrequency Ablation System | Liquid-cooled closed-loop internal cooling | Bipolar |
| Medtronic | Cool-tip™ RF Ablation System E Series | Liquid-cooled closed-loop internal cooling | Single/ Multiple |
| Boston Scientific | Chilli II™ Cooled Ablation Catheter | Liquid-cooled closed-loop internal cooling / Liquid-cooled open perfusion | Single/ Multiple |
| IceCure Medical | The ProSense™ Cryoablation System | Liquid nitrogen internal cooling | Single |
| Surgnova | Dophi™ R150E | Liquid-cooled closed-loop internal cooling | Single/ Multiple |
| Everpace | IceMagic® Cooled ablation equipment | Liquid-cooled open perfusion | Single |

RF, radiofrequency.

potential of MR-guided RFA as a promising option for the treatment of HCC [41]. Collectively, these results suggest that CRFA, enhanced by multiple guidance modalities, is clinically effective in the long-term treatment of HCC and is constantly being explored and innovated to promote the development of local tumor ablation. Additionally, CRFA continues to evolve in other clinical treatments [24, 42-44].

CRFA has emerged as a promising alternative therapy for benign and malignant thyroid nodules. In this outpatient procedure, electrodes are inserted through the skin of the neck under ultrasound guidance to rapidly heat the treatment area. This treatment involves gradually moving the electrodes from the medial to the lateral side of nodule while slowly retracting them toward the surface [45]. Jeong et al. evaluated the safety and efficacy of this approach using internally cooled electrodes and discovered that a remarkable 91.06% of nodules experienced a volume reduction exceeding 50% over a follow-up period ranging from 1 to 41 months, with 27.81% of the nodules completely disappeared [46]. Despite temporary complications such as pain, hematoma, and voice changes, which resolved within one to two months, CRFA was demonstrated to be a safe treatment option for thyroid nodules, although long-term follow-up is necessary to confirm these findings. In another retrospective study by Lim et al., the long-term outcomes of CRFA for benign thyroid nodules were investigated [47]. The study included 111 patients with benign non-functioning nodules, who were treated with a cooled tip radiofrequency system and followed up for a minimum of 3 years. The results demonstrated a mean nodule volume reduction of (93.4 ± 11.7)%, a regeneration rate of 5.6% and an overall complication rate of 3.6%. Furthermore, CRFA has also been effectively used to treat large thyroid nodules, benign thyroid nodules in children and adolescents, small follicular tumors, and even low-risk small thyroid cancers [48-51]. Despite these promising findings, there remains variability in treatment parameters such as the number of sessions, energy delivered, and follow-up duration. Therefore, continued long-term follow-up is needed to validate the safety and efficacy of CRFA. Nevertheless, CRFA holds excellent promise as a safe and effective alternative to surgery for treating thyroid nodules.

CRFA offers a less invasive alternative to surgery for chronic sacroiliac joint pain, producing better outcomes than traditional treatments involving steroid and anesthetic injections. Several case series have reported successful results using CRFA in the sacroiliac joint. Notably, in the study of Kapural et al., they reported retrospective observational data on pain relief and functional changes after denervation with CRFA [52]. Their study, which included 27 patients, revealed a notable reduction in opioid use and clinically significant levels of pain relief and operational improvement at 3-4 months follow-up. Cheng et al. were the first to compare the effectiveness of lateral branch CRFA with conventional RFA for sacroiliac joint pain in a clinical study [53]. In their study, data from

88 patients between January 2006 and June 2009 were retrospectively analyzed, without any evidence showing that lateral branch CRFA provided longer-term relief of sacroiliac joint pain than conventional RFA. However, Tinnirello et al. conducted a follow-up in 43 patients who received CRFA versus conventional RFA to denervate the sacroiliac joint and found that patients receiving CRFA experienced more significant pain relief than patients with traditional RFA [54]. The most remarkable analgesic differences occurred at 6 and 12 months.

In 2016, Cheng et al. further explored the use of bipolar RFA in treating 31 patients with sacroiliac joint pain [55]. Their analysis revealed a cost savings of over $1000 per patient when compared to CRFA. Kurklinsky et al. analyzed the electronic records of 41 adult patients who underwent successful CRFA treatment, and found that the medical costs decreased by 51.0% after the initial CRFA and by 70.4% after subsequent CRFA procedures [56]. Although these studies highlight that CRFA is a promising option for chronic sacroiliac joint pain, more randomized controlled trials are needed to establish its superiority over other radiofrequency denervation options.

In recent years, encouraging advancements have been achieved in treating knee pain associated with osteoarthritis by CRFA. This innovative method uses thermal ablation to disrupt the pain signals transmission by sensory nerves in knee. Lash et al. proved the efficacy of CRFA in relieving pain and improving joint function in 51 patients through precisely locating the target nerve and positioning the electrode needle for surgical intervention under ultrasound guidance [57]. In another study, Davis et al. compared the effectiveness of CRFA and intra-articular steroid injections in treating chronic knee pain among 151 patients [58]. Their findings revealed that CRFA provided significantly better pain relief, with 74.1% of patients experiencing a significant reduction in pain at six months, compared to only 16.2% with intra-articular steroid. Moreover, CRFA offers a long-term treatment option for the control and improvement of knee osteoarthritis. This is evident from studies indicating that 65% and 61% of patients achieved significant pain reduction at 12 and 24 months, respectively [59, 60]. Collectively, these studies underscore the potential of CRFA as an effective and sustainable treatment option for patients suffering from knee pain caused by osteoarthritis.

In addition to its aforementioned clinical applications, CRFA has also shown lasting clinical benefits in treating conditions like osteoid osteoma and cancers of the spine, kidney, heart, hip, lung, pancreas, and breast. CRFA technique outperforms standard RF ablation in overcoming the physiological limitations. By delivering higher energy to the surrounding tissues, it creates larger lesions and more extensive tissue disruption, thus leading to durable clinical outcomes. Nevertheless, comprehensive evaluations including extended follow-up periods and additional research are still crucial for determining overall medical costs, survival rates, local recurrence rates, complication rates, disease-free survival rates, and mortality rates of patients. Such studies are essential to fully understand the clinical implications and long-term benefits of CRFA in these medical applications.

## Conclusion

CRFA represents an improvement in the field of traditional RFA by incorporating air or liquid cooling mechanisms to lower the temperature of the tip of electrode needle during the standard RFA procedure. The cooling technology minimizes the charring of surrounding biological tissues, allowing for the unimpeded and prolonged output of radiofrequency energy, expanding the range of tumor ablation. Currently, most RFA devices in the market are equipped electrode cooling technology, significantly enhancing the safety and effectiveness of tumor treatment.

Numerous clinical applications have demonstrated the feasibility and safety of CRFA as a viable treatment modality. Nonetheless, the ongoing need for further research remains paramount to delve deeper into various aspects of CRFA, including survival rates, local recurrence rates, complication occurrence rates, disease-free survival rates, mortality rates, etc. The ultimate goal of these continued research efforts is to make CRFA more accessible and affordable, ultimately extending its reach to a broader patient population.

**Author contributions:** Dandan Gu collected and summarized materials; wrote and revised the review; created figures and tables. Ruiyan Qian contributed to writing and revised the content. Dani Rui conducted literature review; collected data; created figures and tables. Difang Liu and Haitao Yao proofread the paper. Yifan Yang investigated and compared existing radiofrequency ablation instruments on the market. Yu Zhou provided writing ideas and guided the writing.

## References


[1] Ahmed M, Solbiati L, Brace CL, et al. Image-guided tumor ablation: standardization of terminology and reporting criteria--a 10-year update. J Vasc Interv Radiol 2014;25:1691-1705.e1694.

[2] Fartoux L, Arrive L, Andreani T, et al. Treatment of small hepatocellular carcinoma with acetic acid percutaneous injection. Gastroenterol Clin Biol 2005;29:1213-1219.

[3] Carrafiello G, Laganà D, Mangini M, et al. Microwave tumors ablation: principles, clinical applications and review of preliminary experiences. Int J Surg 2008;6 Suppl 1:S65-69.

[4] Livraghi T, Giorgio A, Marin G, et al. Hepatocellular carcinoma and cirrhosis in 746 patients: long-term results of percutaneous ethanol injection. Radiology 1995;197:101-108.

[5] Park BK, Shen SH, Fujimori M, et al. Thermal Ablation for Renal Cell Carcinoma: Expert Consensus from the Asian Conference on Tumor Ablation. Korean J Radiol 2021;22:1490-1496.

[6] Tatli S, Tapan U, Morrison PR, et al. Radiofrequency ablation: technique and clinical applications. Diagn Interv Radiol 2012;18:508-516.

[7] Habibi M, Berger RD, Calkins H. Radiofrequency ablation: technological trends, challenges, and opportunities. Europace 2021;23:511-519.

[8] Narayanan G, Froud T, Suthar R, et al. Irreversible electroporation of hepatic malignancy. Semin Intervent Radiol 2013;30:67-73.

[9] Kotewall N, Lang BHH. High-intensity focused ultrasound ablation as a treatment for benign thyroid diseases: the present and future. Ultrasonography 2019;38:135-142.

[10] Zachariah C, Mayeux J, Alas G, et al. Physiological and functional responses of water-cooled versus traditional radiofrequency ablation of peripheral nerves in rats. Reg Anesth Pain Med 2020;45:792-798.

[11] Murphy KP, Maher MM, O'Connor OJ. Abdominal Ablation Techniques. AJR Am J Roentgenol 2015;204:W495-W502.

[12] Nguyen DT, Zheng LJ, Zipse MM, et al. Bipolar radiofrequency ablation creates different lesion characteristics compared to simultaneous unipolar ablation. J Cardiovasc Electrophysiol 2019;30:2960-2967.

[13] Clasen S, Schmidt D, Boss A, et al. Multipolar radiofrequency ablation with internally cooled electrodes: Experimental study in ex vivo bovine liver with mathernatic modeling. Radiology 2006;238:881-890.

[14] Knavel EM, Brace CL. Tumor ablation: common modalities and general practices. Tech Vasc Interv Radiol 2013;16:192-200.

[15] Cedeno DL, Vallejo A, Kelley CA, et al. Comparisons of Lesion Volumes and Shapes Produced by a Radiofrequency System with a Cooled, a Protruding, or a Monopolar Probe. Pain Physician 2017;20:E914-E921.

[16] Rempp H, Voigtlander M, Schenk M, et al. Internally gas-cooled radiofrequency applicators as an alternative to conventional radiofrequency and microwave ablation devices: An in vivo comparison. Eur J Radiol 2013;82:E350-E355.

[17] Rempp H, Scharpf M, Voigtlaender M, et al. Sustained Growth of the Ex Vivo Ablation Zones' Critical Short Axis Using Gas-cooled Radiofrequency Applicators. Cardiovasc Intervent Radiol 2011;34:149-155.

[18] Carrara S, Arcidiacono PG, Albarello L, et al. Endoscopic ultrasound-guided application of a new internally gas-cooled radiofrequency ablation probe in the liver and spleen of an animal model: a preliminary study. Endoscopy 2008;40:759-763.

[19] Rempp H, Voigtlander M, Clasen S, et al. Increased Ablation Zones Using a Cryo-Based Internally Cooled Bipolar RF Applicator in Ex Vivo Bovine Liver. Invest Radiol 2009;44:763-768.

[20] Hoffmann R, Bustamante J, Pitsaer C, et al. Forms of Energy Delivery during Cryo-cooled Radiofrequency Ablation for Optimization of the Ablation Result. Rofo 2014;186:945-950.

[21] Schirmang TC, Dupuy DE. Image-guided thermal ablation of nonresectable hepatic tumors using the Cool-Tip (TM) radiofrequency ablation system. Expert Rev Med Devices 2007;4:803-814.

[22] Takaki H, Kodama Y, Miyamoto H, et al. Radiofrequency Ablation by a 21-Gauge Internally Cooled Electrode: Ex Vivo and In Vivo Evaluation by Rat Liver. Cardiovasc Intervent Radiol 2021;44:150-155.

[23] Lorentzen T. A cooled needle electrode for radiofrequency tissue ablation: thermodynamic aspects of improved performance compared with conventional needle design. Acad Radiol 1996;3:556-563.

[24] Solbiati L, Ierace T, Gennaro N, et al. Percutaneous radiofrequency ablation of HCC: reduced ablation duration and increased ablation size using single, internally cooled electrodes with an optimized pulsing algorithm. Int J Hyperthermia 2020;37:861-867.

[25] Yu MH, Lee JY, Jun SR, et al. Radiofrequency Ablation with an Internally Cooled Monopolar Directional Electrode: Ex Vivo and in Vivo Experimental Studies in the Liver. Radiology

2016;278:395-404.
[26] Ni Y, Miao Y, Mulier S, et al. A novel "cooled-wet" electrode for radiofrequency ablation. Eur Radiol 2000;10:852-854.
[27] Cha J, Choi D, Lee MW, et al. Radiofrequency Ablation Zones in Ex Vivo Bovine and In Vivo Porcine Livers: Comparison of the Use of Internally Cooled Electrodes and Internally Cooled Wet Electrodes. Cardiovasc Intervent Radiol 2009;32:1235-1240.
[28] Kim JH, Kim PN, Won HJ, et al. Percutaneous Radiofrequency Ablation with Internally Cooled versus Internally Cooled Wet Electrodes for Small Subphrenic Hepatocellular Carcinomas. J Vasc Interv Radiol 2013;24:351-356.
[29] Cha DI, Lee MW, Jeong WK, et al. Comparison of ablation performance between dual internally cooled wet tip and conventional dual internally cooled tip radiofrequency electrodes: an experimental study in ex vivo bovine liver. Int J Hyperthermia 2021;38:332-340.
[30] Gillams AR, Lees WR. CT mapping of the distribution of saline during radiofrequency ablation with perfusion electrodes. Cardiovasc Intervent Radiol 2005;28:476-480.
[31] Ng KK, Lam CM, Poon RT, et al. Porcine liver: Morphologic characteristics and cell viability at experimental radiofrequency ablation with internally cooled electrodes. Radiology 2005;235:478-486.
[32] Mulier S, Ni Y, Frich L, et al. Experimental and clinical radiofrequency ablation: proposal for standardized description of coagulation size and geometry. Ann Surg Oncol 2007;14:1381-1396.
[33] Gravante G, Ong SL, Metcalfe MS, et al. The effects of radiofrequency ablation on the hepatic parenchyma: histological bases for tumor recurrences. Surg Oncol 2011;20:237-245.
[34] Clasen S, Rempp H, Schmidt D, et al. Multipolar radiofrequency ablation using internally cooled electrodes in ex vivo bovine liver: Correlation between volume of coagulation and amount of applied energy. Eur J Radiol 2012;81:111-113.
[35] Liew J, Salmon L, Mittal R, et al. A pilot study of intraoperative application of cooled radiofrequency to reduce post-operative pain following total knee arthroplasty. Knee 2024;46:62-70.
[36] Pezeshki PS, Woo J, Akens MK, et al. Evaluation of a bipolar-cooled radiofrequency device for ablation of bone metastases: preclinical assessment in porcine vertebrae. Spine J 2014;14:361-370.
[37] Zhang B, Moser MAJ, Zhang EM, et al. A new approach to feedback control of radiofrequency ablation systems for large coagulation zones. Int J Hyperthermia 2017;33:367-377.
[38] Chen MH, Yang W, Yan K, et al. Large liver tumors: protocol for radiofrequency ablation and its clinical application in 110 patients--mathematic model, overlapping mode, and electrode placement process. Radiology 2004;232:260-271.
[39] Rhim H, Lim HK, Kim YS, et al. Percutaneous radiofrequency ablation with artificial ascites for hepatocellular carcinoma in the hepatic dome: Initial experience. Am J Roentgenol 2008;190:91-98.
[40] Tang Z, Fang HQ, Wu YL, et al. Ultrasound-guided percutaneous radiofrequency ablation of hepatic malignancies with cool-tip needle. Zhonghua Zhong Liu Za Zhi 2008;30:706-708.
[41] Clasen S, Rempp H, Boss A, et al. MR-guided Radiofrequency Ablation of Hapatocellular Carcinoma: Long-term Effectiveness. J Vasc Interv Radiol 2011;22:762-770.
[42] Kim JH, Kim PN, Won HJ, et al. Percutaneous Radiofrequency Ablation Using Internally Cooled Wet Electrodes for the Treatment of Hepatocellular Carcinoma. Am J Roentgenol 2012;198:471-476.
[43] Tan TH, Li XS, Wang Q, et al. Percutaneous Radiofrequency Ablation With a Multiple-Electrode Switching System for Medium-Sized Hepatocellular Carcinomas. Int Surg 2021;105:489-496.
[44] Qu CM, Li XQ, Li CF, et al. The Short-Term Efficacy of Novel No-Touch Combined Directional Perfusion Radiofrequency Ablation in the Treatment of Small Hepatocellular Carcinoma with Cirrhosis. J Invest Surg 2022;35:880-887.
[45] Bernardi S, Stacul F, Zecchin M, et al. Radiofrequency ablation for benign thyroid nodules. J Endocrinol Invest 2016;39:1003-1013.
[46] Jeong WK, Baek JH, Rhim H, et al. Radiofrequency ablation of benign thyroid nodules: safety and imaging follow-up in 236 patients. Eur Radiol 2008;18:1244-1250.
[47] Lim HK, Lee JH, Ha EJ, et al. Radiofrequency ablation of benign non-functioning thyroid nodules: 4-year follow-up results for 111 patients. Eur Radiol 2013;23:1044-1049.
[48] Yao ZC, Wu T, Zheng BW, et al. A Novel Strategy for Single-Session Ultrasound-Guided Radiofrequency Ablation of Large Benign Thyroid Nodules: A Pilot Cohort Study. Front Endocrinol (Lausanne) 2020;11:560508.
[49] Ha SM, Sung JY, Baek JH, et al. Radiofrequency ablation of small follicular neoplasms: initial clinical outcomes. Int J Hyperthermia 2017;33:931-937.
[50] Kim JH, Baek JH, Sung JY, et al.

Radiofrequency ablation of low-risk small papillary thyroidcarcinoma: preliminary results for patients ineligible for surgery. Int J Hyperthermia 2017;33:212-219.

[51] Hong MJ, Sung JY, Baek JH, et al. Safety and Efficacy of Radiofrequency Ablation for Nonfunctioning Benign Thyroid Nodules in Children and Adolescents in 14 Patients over a 10-Year Period. J Vasc Interv Radiol 2019;30:900-906.

[52] Kapural L, Nageeb F, Kapural M, et al. Cooled radiofrequency system for the treatment of chronic pain from sacroiliitis: the first case-series. Pain Pract 2008;8:348-354.

[53] Cheng JG, Pope JE, Dalton JE, et al. Comparative Outcomes of Cooled Versus Traditional Radiofrequency Ablation of the Lateral Branches for Sacroiliac Joint Pain. Clin J Pain 2013;29:132-137.

[54] Tinnirello A, Barbieri S, Todeschini M, et al. Conventional (Simplicity III) and Cooled (SInergy) Radiofrequency for Sacroiliac Joint Denervation: One-Year Retrospective Study Comparing Two Devices. Pain Med 2017;18:1731-1744.

[55] Cheng JG, Chen SL, Zimmerman N, et al. A New Radiofrequency Ablation Procedure to Treat Sacroiliac Joint Pain. Pain Physician 2016;19:603-615.

[56] Kurklinsky S, Boone MK, Candler SA, et al. Repeat Cooled Radiofrequency Ablation Is Beneficial for Chronic Posterior Sacroiliac Joint Pain. Pain Med 2020;21:1532-1537.

[57] Lash D, Frantz E, Hurdle MF. Ultrasound-guided cooled radiofrequency ablation of the genicular nerves: a technique paper. Pain Manag 2020;10:147-157.

[58] Davis T, Loudermilk E, DePalma M, et al. Prospective, Multicenter, Randomized, Crossover Clinical Trial Comparing the Safety and Effectiveness of Cooled Radiofrequency Ablation With Corticosteroid Injection in the Management of Knee Pain From Osteoarthritis. Reg Anesth Pain Med 2018;43:84-91.

[59] Davis T, Loudermilk E, DePalma M, et al. Twelve-month analgesia and rescue, by cooled radiofrequency ablation treatment of osteoarthritic knee pain: results from a prospective, multicenter, randomized, cross-over trial. Reg Anesth Pain Med 2019;44:499-506.

[60] Hunter C, Davis T, Loudermilk E, et al. Cooled Radiofrequency Ablation Treatment of the Genicular Nerves in the Treatment of Osteoarthritic Knee Pain: 18-and 24-Month Results. Pain Pract 2020;20:238-246.

Progress in Medical Devices
eISSN: 2957-5478

Zentime

Review Article https://doi.org/10.61189/016816myowlr

# A comprehensive review of spike sorting algorithms in neuroscience

Wentao Quan[1], Youguo Hao[2], Xudong Guo[1], Peng Wang[1], Yukai Zhong[3]

[1]School of Health Science and Engineering, University of Shanghai for Science and Technology, Shanghai 200093, China. [2]Putuo District People's Hospital, Shanghai 200060, China. [3]Yangpu District Kongjiang Hospital, Shanghai 200082, China.

**Corresponding author:** Youguo Hao.

**Acknowledgement:** This work was supported by the Science and Technology Innovation Plan of Shanghai Science and Technology Commission (22S31902200).

**Declaration of conflict of interest:** None.

Received December 17, 2023; Accepted January 15, 2024; Published June 30, 2024

## Highlights

- The detailed steps of spike sorting algorithm and the different algorithms used in each step are summarized.
- The advantages and disadvantages of each step of spike sorting algorithm are compared.
- The detailed application of deep learning technology in spike sorting is introduced.

## Abstract

Spike sorting plays a pivotal role in neuroscience, serving as a crucial step of separating electrical signals recorded from multiple neurons to further analyze neuronal interactions. This process involves separating electrical signals that originate from multiple neurons, recorded through devices like electrode arrays. This is a very important link in the field of brain-computer interfaces. The objective of spike sorting algorithm (SSA) is to distinguish the behavior of one or more neurons from background noise using the waveforms captured by brain-embedded electrodes. This article starts from the steps of the conventional SSA and divides the SSA into three steps: spike detection, spike feature extraction, and spike clustering. It outlines prevalent algorithms for each phase before delving into two emerging technologies: template matching and deep learning-based methods. The discussion on deep learning is further subdivided into three approaches: end-to-end solution, deep learning for spike sorting steps, and spiking neural networks-based solutions. Finally, it elaborates future challenges and development trends of SSAs.

**Keywords**: Spike sorting, spike detection, feature extraction, clustering, deep learning

## Introduction

The control signals currently used in brain-computer interfaces (BCI) mainly include the following five types: action potentials (spike), local field potentials, electrocorticography (ECoG), epidural field potentials, and electroencephalography [1]. The sites where each signal is acquired in the brain are shown in **Figure 1**. **Figure 1** was adapted from [1]. Spike is a key signal reflecting the behavioral activity of the brain, and the study of neuronal information storage and encoding via spike contributes to better development of analog brain computers [2]. There is a close relationship between local field potentials and spike, and their good stability and frequency content provide key advantages for long-term, low-power BCI [3]. ECoG, capturing detailed aspects of actual and imagined body movements, facilitates the development of robust and long-term BCI systems [4]. Compared to ECoG, epidural field potentials are acquired in the epidural space, which greatly reduces the risk of surgical complications, making them suitable for long-term implantation of BCI [5]. though non-invasive and low-cost, offers limited brain activity information, restricting its use to simple communication and

**Address correspondence to: Youguo Hao**, Putuo District People's Hospital, No.1291 Jiangning Road, Putuo, Shanghai 200060, China. Email: youguohao6@163.com.

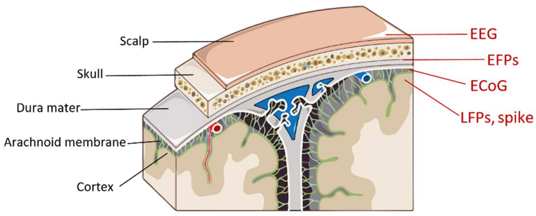


**Figure 1. The locations in the brain where various signals occur.** EEG, electroencephlography; EFPs, eqidural field potentials; ECoG, electrocorticography; LFPs, local field potentials. This Figure was adapted from [1].

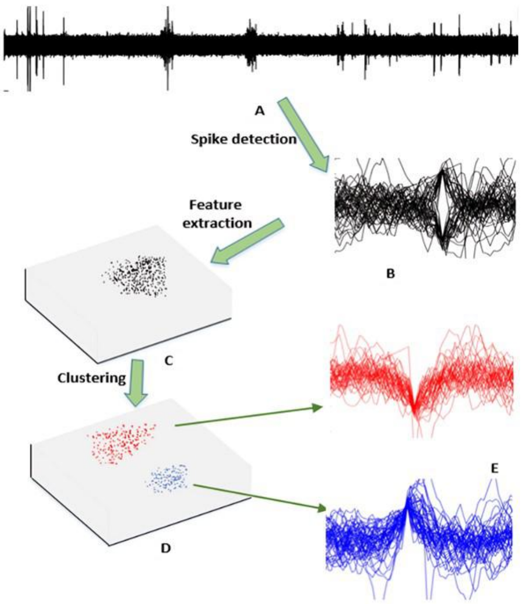


**Figure 2. Basic steps for spike sorting.** (A) A piece of filtered neuronal signal; (B) Spikes are detected, usually using an amplitude threshold of signal; (C) Spike features are extracted to achieve a dimensionality reduction; (D) Clustering operation based on extracted features; (E) The clustering algorithm classifies the waveforms and associates each cluster with a unit. This figure was adapted from [17].

control tasks [6]. Other signals have also been used in BCI, including near-infrared spectroscopy of brain blood flow and functional magnetic resonance imaging. The former's poor spatial resolution and the latter's poor temporal resolution, coupled with high costs, rendering them impractical for widespread application in BCI technologies.

In general, there is a correlation between the level of invasiveness of neural recordings and the quality of signal obtained as well as spatial, spectral, and temporal resolution. The higher the level of invasiveness, the more brain information can be obtained [7]. Spikes, directly emitted by the cells at the implantation site with a frequency range generally between 300Hz and 6000Hz, can reflect the interaction between high-level brain functions and single neurons [8]. Typically, spikes are captured by inserting high-impedance electrodes with a diameter of several microns into the brain, thereby recording neuronal activity near the electrodes in the range of 50-100 microns [9]. In recent years, BCI using spike has attracted increasing interest from scientific community, with the goal of mapping, assisting, enhancing, and repairing cognitive or sensorimotor functions in human or animal brains. Today, spikes are used in the field of BCI to detect pain signals, control robotic arms or wheelchairs, and treat spinal cord injuries [10-12]. However, due to the large amount of spike data and low signal-to-noise ratio (SNR), it has not been widely used clinically.

Since the 1970s, the accurate extraction, detection, and the classification of spikes has been a hot topic in the neuroscience field, known as spike sorting [13]. This review provides a general overview of spike sorting, introduces corresponding algorithms for different steps, and summarizes and compares the current mainstream algorithms. Finally, current study limitations are summarized, and future developments are projected.

## Conventional spike sorting algorithm (SSA)

Spike sorting is an algorithm to detect individual spikes from extracellular neural recordings and classify them based on their shape. The algorithm classifies the detected spikes as originating neurons [14]. The SSA works by dividing different neurons into different clusters, according to their different electrical proximity to the recording electrode and different shapes of dendrites [15]. In theory, a single neuron is represented by a single cluster; however, due to interactions among different neurons, the obtained spike information often overlaps, resulting in a large number of false positives in classification across adjacent channels, thereby complicating accurate categorization [16]. As shown in **Figure 2**, traditional spike sorting has three main steps. **Figure 2** was adapted from [17]. The first step, spike detection, involves identifying spikes at the corresponding time points based on the waveform of each spike. The second step is to extract features corresponding to different spikes and convert them into another feature domain. The final step, spike clustering, is to classify the spikes into different clusters [13].

### *Spike detection*

Spike detection is the initial phase of SSA, dedicated to isolating individual spikes from continuous neural recordings, setting the groundwork for the subsequent stages of the sorting process. Generally, the duration of a spike event is usually 1-3 ms, and the sampling time of each spike event lasts for 30-90 sampling points to prevent spikes from being repeatedly detected. There are currently three mainstream methods of spike detection, including threshold detection method, nonlinear energy operator method, and wavelet transform product method. Each of these methods has its own advantages and disadvantages [17, 18].

*Amplitude thresholding*

The most straightforward algorithm is to apply an amplitude threshold to the spike signal. Since the filtered signal is easily visualized on top of background noise activity, this method is resource-intensive and computationally fast. However, if the applied threshold is too small, noise fluctuations will cause false positive events, and some spikes will be missed. Therefore, setting an adaptive threshold is more suitable.

The most reasonable way is finding a multiple *k* of the noise $\sigma_n$ as the threshold, that is $Thr=k\sigma_n$. The general value of *k* is between 3 and 5. $\sigma_n$ can also be other values. A threshold estimation formula based on the signal median is given [19],

$$Thr = 4 \times median(\frac{|x|}{0.6745}) \qquad (1)$$

where 0.6745 comes from the inverse function of the standard normal distribution cumulative function, which has a value of 0.75. This method processes the background noise according to the standard Gaussian distribution. Even though the noise distribution in real world may deviate from the Gaussian distribution, it has been confirmed that this median-based estimation is more accurate than the standard deviation estimation [20]. However, Equation (1) is not suitable for all situations.

Another study proposed an improved formula [21],

$$Thr = \frac{median\{\frac{|x|}{0.6745}\}\sqrt{2\log_2(n)}}{1.6} \qquad (2)$$

where *n* is the length of the detected data. The addition of *n* into Equation (2) reduces the mixed noise interference introduced by the collection environment, making it more suitable for the adaptive threshold algorithm [21]. However, Equation (2) was later proved to be unsuitable for detection of high noise levels [22]. In this context, Equation (3) was proposed, as follows:

$$Thr = median(\frac{|x|}{0.6745})\sqrt{\frac{\log_2(n)}{n}(\frac{\ln n}{\ln 2})^3 q} \qquad (3)$$

Equation (3) reduces the interference caused by noise fluctuations, making the set threshold more robust. It has been experimentally confirmed that under higher noise levels, the detection accuracy of Equation (3) is significantly higher than Equation (1) and (2) [22].

*Nonlinear energy operator (NEO)*

The NEO is a more powerful detection method, leveraging both frequency and amplitude information. This capability renders NEO more effective than the threshold method in low SNR situations [23]. For the continuous sampling signal *x(n)*, its discrete time NEO $\varphi$ is shown in Equation (4). In addition, some studies suggest using smoothing windows to convolve NEO time series, which can reduce the probability of false positives.

$$\varphi[x(n)] = x^2(n) - x(n+1) \times x(n-1) \qquad (4)$$

$$Thr_{NEO} = \frac{8}{N}\sum_{n=1}^{N}\varphi[x(n)] \qquad (5)$$

Spike is the component with the highest energy in the entire collected signal. Compared with the noise signal, the energy of the spike signal increases instantaneously. This method is ideal for on-chip implementation due to its good transient and computational properties [23]. Malik et al. provided a method for NEO threshold judgment, as shown in Equation (5), whereby a value surpassing this threshold is classified as a spike [24].

*Wavelet transform product*

Wavelet transform has also been proposed for spike detection due to its ability to integrate information from both the time and frequency domains [25]. Compared with the first two methods, the wavelet transform method does not regard the background noise as a standard Gaussian distribution [26]. The principle of this method mainly exploits the fact that the wavelet function is a long "peak" waveform. When sliding wavelet decomposition is used, its essence

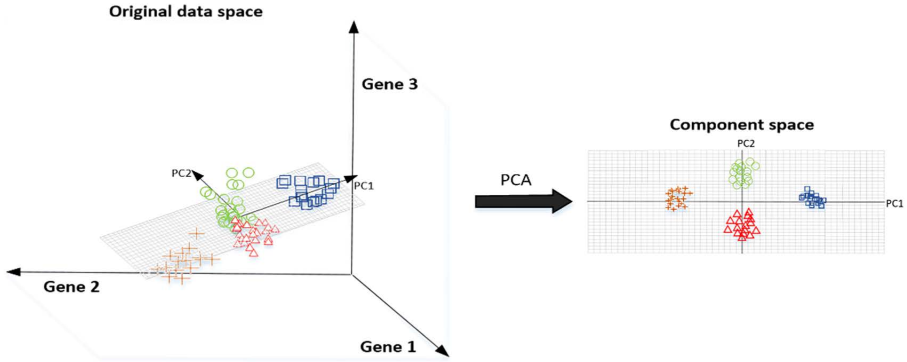


**Figure 3. The process of PCA dimensionality reduction.** PCA, principal component analysis. This Figure was adapted from [42].

is a "template matching" process to evaluate the similarity between the wavelet function and spike. The mathematical definition of wavelet transform is shown in Equation (6), where $\psi$ is the wavelet function, $\tau$ is the translation scale, and α is the scale factor.

$$W(\alpha,\tau)=\int_{-\infty}^{\infty}x(t)\frac{1}{\alpha^{\frac{1}{2}}}\psi(\frac{t-\tau}{\alpha})dt \qquad (6)$$

$$P(n)=\prod_{j=j_{\max}-2}^{j_{\max}}|w(2^{j},n)| \qquad (7)$$

It identifies the signal segment as a spike when there is a relatively high similarity between the signal segment and the wavelet function. There are many choices for wavelet functions in spike detection, such as Haar wavelet, db4 wavelet, and Biorthogonal wavelet. In applications, discrete wavelet transform is generally used, where the value of $\alpha$ is $2^j$*(j=1,2,3...)*. First, the wavelet coefficient $\boldsymbol{w}$ ($\boldsymbol{\alpha}$, $\boldsymbol{\tau}$) corresponding to each $j$ value for each time point is calculated, and all time points until the set maximum $\boldsymbol{j}$ value are summed up, termed as $j_{max.}$ Next, the value of $P$ ($n$) is calculated, which is essentially the product of the wavelet coefficients across three consecutive scales, as shown in Equation (7). Similar to the method described above, using a smoothing window to convolve the $P$ ($n$) sequence can reduce spurious spike due to cross terms and background noise [27, 28].

Among the above three spike detection technologies, since the first two have relatively low computing resource requirements for hardware implementation, they are often favored for online implementation. When the SNR is high and computing resources are limited, the threshold detection method is more suitable. Although the NEO has a simple structure, it necessitates data storage and introduces delays. The first two methods are prone to false positives and false negatives as the noise level changes. Without considering the amount of computing resources, the wavelet transform method can yield the best results [29, 30].

### *Spike feature extraction*

Feature extraction can be performed from three aspects: time domain features, transformation domain features, and dimensionality reduction features. For the time domain features, actual operation can be performed based on the geometric features and derivative features of the spike [31, 32]. For transformation domain features, techniques such as Fourier transform, Hilbert transform, and wavelet transform are employed [33-35]. For dimensionality reduction features, principal component analysis (PCA), linear discriminant analysis (LDA), and Laplacian eigenmaps are utilized [36-38]. After feature extraction, 2 to 3 key features are generally selected and used as inputs in the clustering algorithm to ensure that the next step of the clustering algorithm can be effectively implemented [39, 40]. Several mainstream spike feature extraction algorithms are introduced below.

#### *PCA*

PCA is the most commonly used method in current feature extraction. Its essence is a dimensionality reduction method that projects a data set with multiple relevant features into a coordinate system with fewer relevant features. All detected spike time samples are used as input *x(n)*, and the covariance matrix is eigenvalue decomposed, where the eigenvectors represent the projection direction of the original data. The algorithm mainly includes three steps: (1) creating the covariance matrix of the data set;

(2) calculating all eigenvalues of the covariance matrix and retaining the first k eigenvalues in descending order of variance; (3) transforming the data points through *k* feature vectors [41].

**Figure 3** shows the dimensionality reduction on the original data through PCA. **Figure 3** was adapted from [42]. The disadvantage of this method is its tendency to lose information as the complexity of the collected spike data increases. It is stated that when a higher ***k*** value is selected, the variance of the higher component may be affected by the background noise, so this method is not suitable for feature extraction where the spike information is rich [13].

*Features of wavelet transform*

Wavelet transform is an integral transform that decomposes a specific signal into the sum of different wavelet signals. The relevant equations of wavelet transform are presented in Section 2.1.3. Through the low-frequency and high-frequency wavelet coefficients, it can accurately depict the spike shape [43]. Generally, wavelet transform convolves the original signal with wavelet functions of different parameters derived from the mother wavelet, which can quantify the details of the signal at different resolutions [35]. Haar wavelet and Daubechies wavelet are the two most commonly used mother wavelets in analyzing neurophysiological signals due to their orthogonality. They are able to identify the characteristics of a spike through a few wavelet coefficients without making a priori assumptions about the shape of the spike [19, 44, 45].

The features that can be extracted from the time spectrum mainly include extreme value features and energy distribution features. The former is the most prevalent feature, involve extracting the peak amplitude across each scale and correlating them with the corresponding scale parameters and translation parameters to construct a comprehensive feature vector. The latter requires calculating the energy distribution of each scale space from the energy spectrum, and then identifying the corresponding scale parameters and translation parameters to form the feature vector [46].

*LDA*

LDA is a linear projection technology that seeks a suitable projection direction within a low-dimensional space, so as to maximize the distance between different categories and minimize the distance between the same categories [47]. LDA first calculates the covariance matrix of the data and performs eigenvalue decomposition of the covariance matrix. Then, a projection matrix is formed based on the obtained eigenvectors and eigenvalues to map the original data into a new low-dimensional space [48]. LDA needs to clearly minimize the inter-class variance and maximize the inter-class variance, which are shown in Equation (8) and Equation (9), respectively. Here, $x_i$ is the *ith* data point in the *kth* cluster *ck, μk* represents the average of data points in the *kth* cluster, *μ* represents the average of all data points, and *n* is the total number of data.

$$S_W = \sum_{k=1}^{K} \sum_{x_i \in c_k}^{n_k} (x_i - \mu_k)(x_i - \mu_k)^T \tag{8}$$

$$S_b = \frac{\sum_{k=1}^{K} n_k (\mu_k - \mu)(\mu_k - \mu)^T}{n} \tag{9}$$

LDA has demonstrated its effectiveness in separating spike features, especially when the SNR is low [48].

Unlike PCA, which simplifies high-dimensional data into two or three dimensions without significant information loss and facilitates visualization and classification identification, LDA optimizes dimensionality reduction to avoid overfitting. Wavelet transform can extract detailed features in the spike without too much information loss. However, PCA does not account for the categorical relationships between data points and relies solely on variance for determining principal components, leading to potential information loss. The classification effectiveness of LDA can easily be compromised when there is a great overlap between the data distribution of different categories. Wavelet transform is easily affected by noise, thus selecting suitable parameters for the wavelet basis function is essential [49-51].

***Spike clustering***

Spike clustering refers to organizing points in the feature space into clusters. Each cluster is associated with a different neuron, separated by defined boundaries between different clusters [52]. Optimal clustering techniques should minimize user intervention and achieve efficient and accurate results. It is generally believed that the changes within the cluster are caused by the noise superimposed on the real spike waveform [53]. The background noise obeys the Gaussian distribution. Therefore, most clustering algorithms are built based

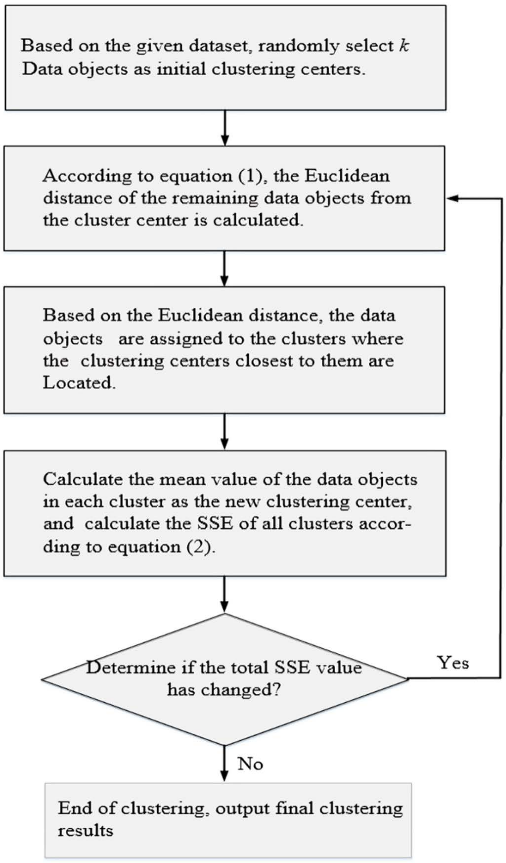


**Figure 4. K-means algorithm flow chart.** SSE, sum of squared error. This figure was adapted from [53].

on the Gaussian model. Most SSAs perform clustering by fitting a Gaussian mixture model, modeling the feature density curve as a sum of Gaussians, or fitting a mixture of t distributions. Several clustering methods commonly used in recent years are introduced.

*K-means*

K-means clustering is one of the prevalent unsupervised learning techniques. It primarily uses the Euclidean distance $d(x,c_i)$ as an indicator to measure the similarity between data objects. Its calculation formula is shown in Equation (10), where $x$ is the data object, $c_i$ is the *ith* cluster center, and $m$ is the dimension of the data. The similarity is inversely proportional to the distance between data objects.

$$d(x,C_i)=\sqrt{\sum_{j=1}^{m}(x_j-C_{ij})^2} \tag{10}$$

$$SSE=\sum_{i=1}^{k}\sum_{x\in C_i}|d(x,C_i)|^2 \tag{11}$$

The algorithm needs to specify the initial number of clusters k and k initial cluster centers in advance. Then, based on the similarity between the data object and the cluster center, the location of the cluster center is continuously updated, and the sum of squared error of the cluster is reduced, as shown in Equation (11). When the sum of squared error no longer changes or the objective function converges, clustering ends and the final result is obtained [54, 55]. The K-means algorithm is a continuously iterative process, and its algorithm flow is shown in **Figure 4. Figure 4** was adapted from [53].

*Mean shift*

Mean shift is a non-parametric clustering method first proposed by Fukunaga and Hostetler [56]. It treats data samples as empirical representations of probability density functions in a *d*-dimensional feature space. Dense regions in the *d*-dimensional feature space is used to represent local maxima of the underlying distribution [57]. The algorithm first estimates the kernel density function, as shown in Equation (12), where *k* represents the symmetrical kernel function, which usually is a Gaussian function.

$$f(x)=\sum_{i}k(\frac{||x-x_i||^2}{h^2}) \tag{12}$$

After each data point is assigned to the corresponding *f(x)*, the algorithm moves the data point to the KDF mapping according to the gradient function in Equation (13) [58].

$$\nabla f(x)=\frac{2c_{k,d}}{nh^{d+2}}[\sum_{i=1}^{n}k'(||\frac{x-x_i}{h}||)][\frac{\sum_{i=1}^{n}x_ik'(||\frac{x-x_i}{h}||^2)^{n}}{\sum_{i=1}^{n}k'(||\frac{x-x_i}{h}||^2)}-x] \tag{13}$$

The focus of the mean shift algorithm is primarily to improve calculation efficiency and robustness [15]. In recent research, Yang et al. proposed a method that combines the mean shift algorithm with the optical flow method, which reduces the cumulative error and thereby improves computational efficiency [59].

*Super-paramagnetic clustering (SPC)*

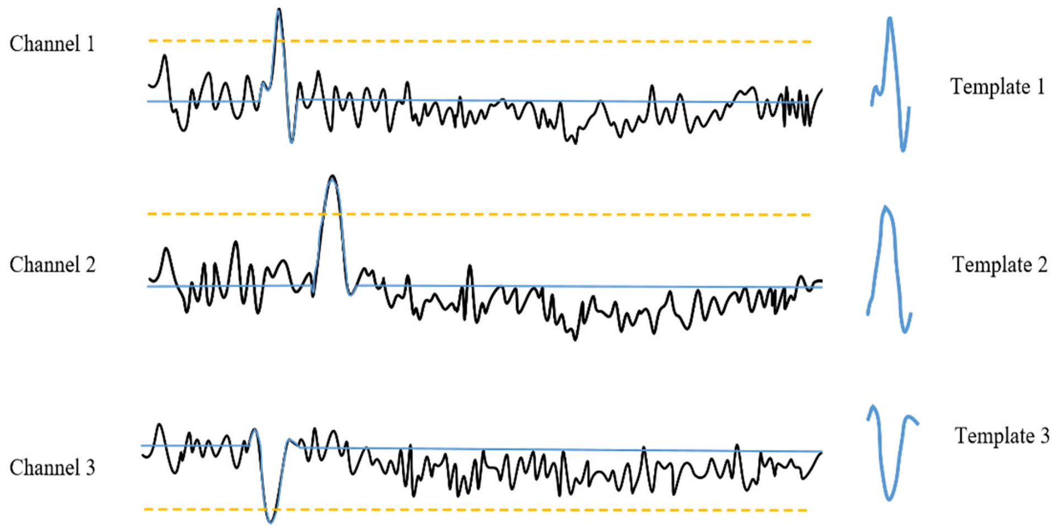


**Figure 5. Templates are obtained using threshold detection method.** This figure was adapted from [15].

SPC is an unsupervised classification technique based on clustering self-tenancy of data density and interaction energy. Drawing inspiration from the interactions observed among superparamagnetic particles under varying temperatures, SPC distinguishes itself from conventional algorithms by excluding the use of clustering distribution functions. First, it uses Equation (14) to mathematically simulate the interaction between $x_i$ and $x_j$ at different points, where a is the average distance between nearest neighbor points. Then, it assigns a "Potts spin" state variable *s* from  to *q* to each point $x_i$, where *q* is usually chosen to be 20. Finally, it uses the Wolff algorithm to perform N Monte Carlo iterations at different temperatures [19, 60]. The state value $p_{ij}$ is updated according to Equation (15), where *T* represents the temperature value.

$$J_{ij} = \frac{1}{k}\exp[-\frac{|x_i - x_j|^2}{2a^2}] \qquad (14)$$

$$P_{ij} = 1 - \exp(-\frac{J_{ij}}{T}\delta_{s_i,s_j}),\ \delta_{s_i,s_j} = \begin{cases} 1 & if\ s_i = s_j \\ 0 & otherwise \end{cases} \qquad (15)$$

$$G_{ij} = \frac{(q-1)c_{ij} + 1}{q} \qquad (16)$$

*s* will be iteratively updated according to the value of $p_{ij}$ until it becomes stable. Equation (16) introduces the spin-spin correlation function, where $c_{ij}$ is a number belonging to the interval [0, 1]. An appropriate threshold ε can be selected. When $G_{ij}$>ε , different data points $x_i$ and $x_j$ belong to the same cluster.

*Fuzzy C-means (FCM)*

FCM combines the K-means algorithm with fuzzy logic, which has good processing effects on data with high complexity. FCM is an iterative algorithm whose execution steps are similar to K-means. First, the number of clusters *k* needs to be determined. Its value can be fixed or adaptive. Next, it randomly initializes the value $\mu_{ij}$ of the cluster member of each point $x_i$ relative to the cluster center $C_j$, and then calculates the cluster center according to Equation (17) [15, 61].

$$C_j \quad \frac{\sum_{i\ 1}^{D} \mu_{ij}{}^{m} x_i}{\sum_{i\ 1}^{D} \mu_{ij}{}^{m}} \qquad (17)$$

$$\mu_{ij} = \frac{1}{\sum_{k=1}^{N}\left(\frac{\|x_i - c_j\|}{\|x_i - c_k\|}\right)^{\frac{2}{m-1}}} \qquad (18)$$

where *D* is the number of data points, and *N* is the number of clusters, and *m* is the fuzzy parameter. The values of cluster members are then calculated and updated using Equation (18), where *m* is a parameter greater than 1. When *m* approaches 1, the ambiguity decreases, and the algorithm result approaches the

K-means algorithm.

Of the four algorithms introduced above, K-means has the simplest structure and is easy to implement, excelling in efficiency with large datasets. Mean shift has good adaptability to data with linear structure. SPC stands out for good adaptability to automatically determine the number of clusters. FCM is distinguished by its good robustness in data processing and has good adaptability to situations where data points belong to multiple clusters. However, each algorithm has its limitations: K-means is sensitive to noise and outliers, and thus does not have good robustness; Mean shift has high computational complexity on large-scale data sets; SPC is complex and can be affected by temperature, and the convergence speed of FCM is relatively slow [62-65].

### Novel SSAs

Novel SSAs do not follow the three steps of traditional algorithms. For example, using neural system simulation and deep shrinkage automatic encoding methods to perform spike sorting [66, 67]. Current mainstream algorithms can perform two or more steps simultaneously, thereby improving algorithm efficiency. These algorithms are mainly divided into two categories, one is template matching and the other is deep learning.

#### *Template matching*

Template matching identifies the position of a specific template within a signal sequence, facilitating accurate and efficient locate specific spikes in spike sorting. It takes the normalized-template-matching method proposed as an example [68]. Firstly, conventional SSAs are used to extract the initial template, such as threshold detection, as shown in **Figure 5**. The figure was adapted from [15]. Subsequently, the template was used to move against the neural recording to assess waveform similarity that determined by calculating the relationship between the extracellular voltage signal and the average spike waveform of each candidate single unit, which here called cross-correlation. Let the average spike waveform of all channels be $\mu_i$, where $\mu_i=[\mu_{i,1},\mu_{i,2},...\mu_{i,N}]$, $\mu_{i,n}$ is at the average spike wave in $n$ channels. Let the $L=f_s k$, where $f_s$ is the sampling frequency and $k$ is the length of the custom time window, then $\mu_{i,n}$ is a $1\times L$ vector. In the same way, the neural recording signal is defined as a vector $u_{i,n}$ that changes with time, thus obtaining $V(t)=[u(t)_1,u(t)_2,...u(t)_N]$. Based on the above, the cross-correlation equation can be obtained:

$$C_i(t) = V(t) \times \mu_i^T \qquad (19)$$

Based on cross-correlation, the two steps of spike detection and feature extraction can be accomplished, and then K-means and other methods can be employed to complete clustering and the entire SSA step. However, since neural recording signals are usually non-stationary, template matching methods require template recalibration over a period of time.

Recent advancements in template matching for peak sorting include the utilization of particle swarm optimization algorithm and the multi-template matching method to optimize the template [69, 70]. For the optimized template, experimental results demonstrated that it could significantly reduce the occurrence of false positives and false negatives. Another study combined templates with convolutional neural networks (CNNs), employing CNNs to train on real spikes and overlapping spikes, which allows for correct spike classification and minimizes the occurrence of repeated spikes [71].

#### *Deep learning*

Deep learning is a popular technology that has been used in various fields for several years. It involves the application of machine learning through deep artificial neural networks (ANN), which has more layers, parameters and neurons. The use of deep learning methods to solve the peak sorting problem has become a popular research direction, and there are three main strategies: (1) end-to-end solution, (2) deep learning for spike sorting steps, and (3) spiking neural network (SNN)-based solutions [72-74].

##### *End-to-end solution*

The end-to-end solution uses the filtered neural recording as the input of the deep neural network and directly outputs the spike sequences produced by different neurons. This approach eliminates tedious preprocessing steps by starting from raw data as input. For instance, researchers used CNN and long short-term memory to perform peak sorting in an end-to-end manner [75]. Here, CNN is used for spike detection, and long short-term memory is used to receive the output stream of CNN and process the corresponding information. Other researchers proposed a medium 1D-CNN model tailored for single-channel spike sorting [76]. Although the end-to-end solution is a simple and efficient way, its internal parameters require a large amount of data for training, and this method is not suitable for complex spikes.

*Deep learning for spike sorting steps*

Section 2 explains spike sorting as a process comprised three independent steps. Some of these steps can be improved by using deep learning methods. The most common one is to use deep learning for spike detection and denoising. Extracellular nerve signal recording contains a variety of components originating from the signal recording equipment or the measured organism itself, such as the activity of nearby neuronal cells. These noises can affect the detection accuracy. Lecoq et al. used original noise samples to train a spatiotemporal nonlinear difference model, thereby achieving the effect of eliminating independent noise sources in the input signal [77]. Okreghe et al. proposed a deep spike detection technique using CNN in conjunction with K-means, exhibiting robust learning capabilities for high-dimensional vectors and effective removal of artifacts in the acquisition channel [78].

*SNN-based solutions*

SNN, a relatively new type of neural network, exhibits functions more akin to neural networks in living organisms when compared to other conventional neural networks. SNN uses a temporal encoding scheme to encode information into spike sequences. It has more powerful information representation capabilities than ANN, especially for complex temporal or spatiotemporal data. In hardware implementation, SNN can achieve fast and large-scale parallel information processing [79, 80]. In the application of spike sorting, Mukhopadhyay et al. proposed a spike sorting method that combines SNN and K-means to achieve training and classification of on-chip systems through a two-step shared training scheme [81]. Werner et al. proposed a method to implement spike sorting using a two-layer SNN. In this technology, there is no need for preliminary waveform detection. The first layer is used to filter the original signal, and the second layer is used for detection and feature extraction. Both layers of neurons follow the Leaky Integrate-and-Fire model [82]. The disadvantage of this technology is that the parameters of Leaky Integrate-and-Fire need to be manually adjusted to adapt to different shapes of waveforms. Later, Bernert et al. optimized it and confirmed the high efficiency of this technology in high-density electrode settings [83].

## Conclusion

This review provides a detailed introduction of various steps involved in SSA, covering the predominant algorithms associated with each step and their current research status. Additionally, a detailed description of the application of deep learning technology in the field of spike sorting is provided. With the development of BCI, there is an escalating demand for enhanced neural signal acquisition channels and signal quality, which also poses challenges to the development of SSAs.

The foremost challenge is to solve the problem of signal non-stationarity. Neural signals change over time and can be affected by multiple factors, leading to temporal variations in spike shapes, especially in systems that require manual intervention [84, 85]. The second challenge is overlapping spikes, which significantly reduce the performance of conventional clustering algorithms [86]. The most commonly accepted solutions nowadays are Bayesian statistical techniques and template matching introduced in section 3.1 and the ANN. However, the above methods are computationally intricate and demand substantial hardware capabilities. Therefore, future research should aim to simplify and enhance the efficiency of algorithms designed to tackle overlapping spikes. The third challenge is the determination of the training data set and evaluation scheme. Most current spike sorting systems are evaluated using synthetic datasets with real labels. The simplest method is to add modeled Gaussian noise to the spike waveform. Due to the interactions between neuronal cells, it is very challenging to form realistic multi-channel synthetic data.

**Author Contributions:** Wentao Quan was responsible for writing and revising the entire article as well as organizing and summarizing relevant information. Youguo Hao was responsible for notification of manuscript status and review of manuscript content. Xudong Guo was responsible for conducting research on “Spike Feature Extraction”. Peng Wang was responsible for conducting research on “spike clustering”. Yukai Zhong was responsible for conducting research on “Novel Spike Sorting Algorithm”.

## References

[1] Slutzky MW, Flint RD. Physiological properties of brain-machine interface input signals. J Neurophysiol 2017;118(2):1329-1343.

[2] Wang JH, Cui S. Neuronal Signal Encoding and Storage as Principles of Brain Function. Prog

Biochem Biophys 2016;43:367-373.
[3] Jackson A, Hall TM. Decoding Local Field Potentials for Neural Interfaces. IEEE Trans Neural Syst Rehabil Eng 2017;25(10):1705-1714.
[4] Schalk G, Leuthardt EC. Brain-computer interfaces using electrocorticographic signals. IEEE Rev Biomed Eng 2011;4:140-154.
[5] Branco MP, Geukes SH, Aarnoutse EJ, et al. Nine decades of electrocorticography: A comparison between epidural and subdural recordings. Eur J Neurosci 2023;57(8):1260-1288.
[6] Wang Y, Nakanishi M, Zhang D. EEG-Based Brain-Computer Interfaces. Adv Exp Med Biol 2019;1101:41-65.
[7] Markowitz DA, Wong YT, Gray CM, et al. Optimizing the Decoding of Movement Goals from Local Field Potentials in Macaque Cortex. J Neurosci 2011;31(50):18412-22.
[8] Franke F, Natora M, Boucsein C, et al. An online spike detection and spike classification algorithm capable of instantaneous resolution of overlapping spikes. J Comput Neurosci 2010;29(1-2):127-148.
[9] Quiroga RQ. What is the real shape of extracellular spikes? J Neurosci Methods 2009;177:194-198.
[10] Hu SL, Zhang QS, Wang J, et al. A Real-Time Rodent Neural Interface for Deciphering Acute Pain Signals from Neuronal Ensemble Spike Activity. 2017 51st Asilomar Conference on Signals, Systems, and Computers 2017;93-97.
[11] Odoherty JE, Merolla PA, Even CN. Brain-machine interface (BMI) with user interface (UI) aware controller. US patent US11630516. 2023/04/18.
[12] Oweiss K, Aghogolzadeh M. Multiscale intra-cortical neural interface system. US patent US2011307079. 2011/12/15.
[13] Lewicki MS. A review of methods for spike sorting: the detection and classification of neural action potentials. Network 1998;9:R53-R78.
[14] Lefebvre B, Yger P, Marre O. Recent progress in multi-electrode spike sorting methods. J Physiol Paris 2016;110:327-335.
[15] Zhang T, Azghadi MR, Lammie C, et al. Spike sorting algorithms and their efficient hardware implementation: a comprehensive survey. J Neural Eng 2023;20 (2).
[16] Marre O, Amodei D, Deshmukh N, et al. Mapping a Complete Neural Population in the Retina. J Neurosci 2012;32:14859-14873.
[17] Hennig MH, Hurwitz C, Sorbaro M. Scaling Spike Detection and Sorting for Next-Generation Electrophysiology. Adv Neurobiol 2019;22:171-184.
[18] Rey HG, Pedreira C, Quian Quiroga R. Past, present and future of spike sorting techniques. Brain Res Bull 2015;119:106-117
[19] Quiroga RQ, Nadasdy Z, Ben-Shaul Y. Unsupervised spike detection and sorting with wavelets and superparamagnetic clustering. Neural Comput 2004;16:1661-1687.
[20] Quiroga RQ. Spike sorting. Curr Biol 2012;22:R45-R46.
[21] Wang J, Guo TX, Lu YS, et al. Heuristic Threshold Detection Algorithm for Spike. Comput Eng Appl 2022;58:192-196.
[22] Zhao DC, Jiao SY, Chen H, et al. Heuristic adaptive threshold detection method for neuronal spikes. IET Signal Process 2023;e12214.
[23] Mukhopadhyay S, Ray GC. A new interpretation of nonlinear energy operator and its efficacy in spike detection. IEEE Trans Biomed Eng 1998;45:180-187.
[24] Malik MH, Saeed M, Kamboh AM. Automatic Threshold Optimization in Nonlinear Energy Operator Based Spike Detection. 2016 38th Annual International Conference of the IEEE Engineering in Medicine and Biology Society (EMBC) 2016;774-777.
[25] Kim KH, Kim SJ. A wavelet-based method for action potential detection from extracellular neural signal recording with low signal-to-noise ratio. IEEE Trans Biomed Eng 2003;50:999-1011.
[26] Nenadic Z, Burdick JW. Spike detection using the continuous wavelet transform. IEEE Trans Biomed Eng 2005;52:74-87.
[27] Shen Q, Liu XY, Jiang DZ. Using modulus maximum pair of wavelet transform to detect spike wave of epileptic EEG. Proceedings of the 20th Annual International Conference of the IEEE Engineering in Medicine and Biology Society. Vol.20 Biomedical Engineering Towards the Year 2000 and Beyond (Cat. No.98CH36286). IEEE, 1998;1543-1545.
[28] Yuning Y, Kamboh A, Andrew JM. Adaptive threshold spike detection using stationary wavelet transform for neural recording implants. 2010 IEEE Biomedical Circuits and Systems Conference (BioCAS 2010) 2010;9-12.
[29] Paralikar KJ, Rao CR, Clement RS. New approaches to eliminating common-noise artifacts in recordings from intracortical microelectrode arrays: Inter-electrode correlation and virtual referencing. J Neurosci Methods 2009;181:27-35.
[30] Rakshit A, Okkesim S, Hofmann UG, et al. Assessing Ambiguity Of Spike Detection By Thresholding. 2023 11th International IEEE/EMBS Conference on Neural Engineering (NER) 2023;1-4.
[31] Zamani M, Demosthenous A. Feature

Extraction Using Extrema Sampling of Discrete Derivatives for Spike Sorting in Implantable Upper-Limb Neural Prostheses. IEEE Trans Neural Syst Rehabil Eng 2014;22:716-726.
[32] Kamboh AM, Mason AJ. Computationally Efficient Neural Feature Extraction for Spike Sorting in Implantable High-Density Recording Systems. IEEE Trans Neural Syst Rehabil Eng 2013;21:1-9.
[33] Yang CH, Yuan Y, Si JN. Robust spike classification based on frequency domain neural waveform features. J Neural Eng 2013;10:066015.
[34] Zhu JD, Lin CF, Chang SH, et al. Analysis of spike waves in epilepsy using Hilbert-Huang transform. J Med Syst 2015;39:170.
[35] Mallat SG. A theory for multiresolution signal decomposition: the wavelet representation. IEEE Trans Pattern Anal Mach Intell 1989;11:674-693.
[36] Zhao DC, Jiao SY, Li L, et al. Neuron spike classification method, involves obtaining original spike signal and preprocess obtained spike signal, and reducing dimensionality of spike data by principal component analysis to obtain eigenvalues and eigenvectors, and map spike points to feature space constructed by the eigenvectors. China patent CN115844422A. 2023/03/28.
[37] Chen W, Shen CP, Chiu MJ, et al. Epileptic EEG Visualization and Sonification Based on Linear Discriminate Analysis. 2015 37th Annual International Conference of the IEEE Engineering in Medicine and Biology Society (EMBC) 2015;4466-4469.
[38] Liu F, Zhang WJ, Gu SC. Local linear Laplacian eigenmaps: A direct extension of LLE. Pattern Recogn Lett 2016;75:30-35.
[39] Wang T. Characteristic of Neural Signal Feature for Spike Sorting and Detection. J Phys Conf Ser 2021;2078:012042.
[40] Huang L, Gan L, Ling BW. A Unified Optimization Model of Feature Extraction and Clustering for Spike Sorting. IEEE Trans Neural Syst Rehabil Eng. 2021;29:750-759.
[41] Wheeler BC, Heetderks WJ. A comparison of techniques for classification of multiple neural signals. IEEE Trans Biomed Eng 1982;29:752-759.
[42] Visualization of PCA principal component analysis. Available at: https://zhuanlan.zhihu.com/p/28909807
[43] Lieb F, Stark HG, Thielemann C. A stationary wavelet transform and a time-frequency based spike detection algorithm for extracellular recorded data. J Neural Eng 2017;14:036013.
[44] Hulata E, Segev R, Ben-Jacob E. A method for spike sorting and detection based on wavelet packets and Shannon's mutual information. J Neurosci Methods 2002;117:1-12.
[45] Letelier JC, Weber PP. Spike sorting based on discrete wavelet transform coefficients. J Neurosci Methods 2000;101:93-106.
[46] Wang PSP, Yang JW. A Review of Wavelet-Based Edge Detection Methods. Int J Pattern Recognit Artif Intell 2012;26(07):1255011.
[47] Sifaou H, Kammoun A, Alouini MS. High-dimensional Linear Discriminant Analysis Classifier for Spiked Covariance Model. J Mach Learn Res 2020;21:4508–4531.
[48] Keshtkaran MR, Yang Z. Noise-robust unsupervised spike sorting based on discriminative subspace learning with outlier handling. J Neural Eng 2017 ;14:036003.
[49] Chah E, Hok V, Della-Chiesa A, et al. Automated spike sorting algorithm based on Laplacian eigenmaps and k-means clustering. J Neural Eng 2011;8:016006.
[50] Quiroga RQ, Panzeri S. Extracting information from neuronal populations: information theory and decoding approaches. Nat Rev Neurosci 2009;10:173-185.
[51] Rossant C, Kadir SN, Goodman DFM, et al. Spike sorting for large, dense electrode arrays. Nat Neurosci 2016;19:634-641.
[52] Carlson D, Carin L. Continuing progress of spike sorting in the era of big data. Curr Opin Neurobiol 2019;55:90-96.
[53] Pouzat C, Mazor O, Laurent G. Using noise signature to optimize spike-sorting and to assess neuronal classification quality. J Neurosci Methods 2002;122:43-57.
[54] Yang J, Zhao C. Survey on K-Means Clustering Algorithm. Comput Eng Appl 2019;55:7-14, 63.
[55] Jain AK. Data clustering: 50 years beyond K-means. Pattern Recogn Lett 2010;31:651-666.
[56] Fukunaga K, Hostetler LD. The estimation of the gradient of a density function, with applications in pattern recognition. IEEE T Inform Theory 1975;21:32-40.
[57] Nguyen T, Khosravi A, Hettiarachchi I, et al. Classification of Neural Action Potentials using Mean Shift Clustering. 2014 IEEE International Conference on Systems, Man, and Cybernetics (SMC) 2014;1247-1252.
[58] Comaniciu D, Meer P. Mean shift: A robust approach toward feature space analysis. IEEE Trans Pattern Anal Mach Intell 2002;24:603-619.
[59] Yang X, Li Q, He C. Improved Meanshift Tracking Algorithm Based on Optical flow. 2023 IEEE 6th Eurasian Conference on Educational Innovation (ECEI) 2023;159-162.
[60] Wang PK, Chen CH, Pun SH, et al. Parallel architecture to accelerate superparamagnetic clustering algorithm. Electron Lett 2020;56:701-704.
[61] Inan ZH, Kuntalp M. A study on fuzzy C-means

clustering-based systems in automatic spike detection. Comput Biol Med 2007;37:1160-1166.
[62] Hamed HNA, Saleh AY, Shamsuddin SMH, et al. Multi-objective K-means evolving spiking neural network model based on differential evolution. 2015 International Conference on Computing, Control, Networking, Electronics and Embedded Systems Engineering (ICCNEEE) 2015;379-383.
[63] Yang Z, Zhao Q, Liu WT, et al. Energy Based Evolving Mean Shift Algorithm for Neural Spike Classification. 2009 Annual International Conference of the IEEE Engineering in Medicine and Biology Society 2009;966-969.
[64] Ott T, Kern A, Stoop R. Faster spike sorting with belief propagation. 2006 International Symposium on Nonlinear Theory and its Applications 2006;1027-1030.
[65] Lin R, Lin J, Wang J, et al. Diagnosing transformer voiceprint fault based on fuzzy C-means clustering algorithm comprises using fuzzy C-means clustering algorithm to classify different voiceprint fault data, and using classification results to determine type of fault. China patent CN112149569A. 2020/12/29.
[66] Yu H, Qi Y, Pan G. NeuSort: an automatic adaptive spike sorting approach with neuromorphic models. J Neural Eng 2023;20.
[67] Radmanesh M, Rezaei AA, Jalili M, et al. Online spike sorting via deep contractive autoencoder. Neural Networks 2022;155:39-49.
[68] Laboy-Juárez KJ, Ahn S, Feldman DE. A normalized template matching method for improving spike detection in extracellular voltage recordings. Sci Rep 2019;9:12087.
[69] Wu DP, Shi HC, Jiang LR, et al. BECT Spike Detection Algorithm Based on Optimal Template Matching and Morphological Feature Selection. IEEE Trans Circuits Syst II Express Briefs 2022;69:2366-2370.
[70] Jiang TJ, Wu DP, Gao F, et al. Improved Spike Detection Algorithm Based on Multi-Template Matching and Feature Extraction. IEEE Trans Circuits Syst II Express Briefs 2022;69:249-253.
[71] Zhang L, Gao D, Wang M. Sorting Overlapping Spikes Based on Log-Mel Spectrogram and Convolutional Neural Networks. 2023 6th International Conference on Artificial Intelligence and Big Data (ICAIBD) 2023;482-485.
[72] Wu T, Zhao W, Keefer E, et al. Deep Compressive Autoencoder for Action Potential Compression in Large-Scale Neural Recording. J Neural Eng 2018;15:066019.
[73] Wouters J, Kloosterman F, Bertrand A. A data-driven spike sorting feature map for resolving spike overlap in the feature space. J Neural Eng 2021;18.
[74] Buccino AP, Garcia S, Yger P. Spike sorting: new trends and challenges of the era of high-density probes. Prog Biomed Eng 2022;4:022005.
[75] Rácz M, Liber C, Németh E, et al. Spike detection and sorting with deep learning. J Neural Eng 2020;17:016038.
[76] Li ZH, Wang YT, Zhang N, et al. An Accurate and Robust Method for Spike Sorting Based on Convolutional Neural Networks. Brain Sci 2020;10:835.
[77] Lecoq J, Oliver M, Siegle JH, et al. Removing independent noise in systems neuroscience data using DeepInterpolation. Nat Methods 2021;18:1401-1408.
[78] Okreghe CO, Zamani M, Demosthenous A. A Deep Neural Network-Based Spike Sorting With Improved Channel Selection and Artefact Removal. IEEE Access 2023;11:15131-15143.
[79] Wang XW, Lin XH, Dang XC. Supervised learning in spiking neural networks: A review of algorithms and evaluations. Neural Networks 2020;125:258-280.
[80] Farsa EZ, Ahmadi A, Maleki MA, et al. A Low-Cost High-Speed Neuromorphic Hardware Based on Spiking Neural Network. IEEE Trans Circuits Syst II Express Briefs 2019;66:1582-1586.
[81] Kumar Mukhopadhyay A, Chakrabarti I, Basu A, et al. Power efficient Spiking Neural Network Classifier based on memristive crossbar network for spike sorting application. arXiv:1802.09047.
[82] Werner T, Vianello E, Bichler O, et al. Spiking Neural Networks Based on OxRAM Synapses for Real-Time Unsupervised Spike Sorting. Front Neurosci 2016;10:474.
[83] Bernert M, Yvert B. An Attention-Based Spiking Neural Network for Unsupervised Spike-Sorting. Int J Neural Syst 2019;29:1850059.
[84] Fee MS, Mitra PP, Kleinfeld D. Variability of extracellular spike waveforms of cortical neurons. J Neurophysiol 1996;76:3823-3833.
[85] Snider RK, Bonds AB. Classification of non-stationary neural signals. J Neurosci Methods 1998;84:155-166.
[86] Harris KD, Henze DA, Csicsvari J, et al. Accuracy of tetrode spike separation as determined by simultaneous intracellular and extracellular measurements. J Neurophysiol 2000;84:401-414.

Progress in Medical Devices
eISSN: 2957-5478

Review Article https://doi.org/10.61189/579429fwpcmo

# Research progress of photoacoustic imaging technology in brain diseases

Tingting Shi, Rongguo Yan, Xinrui Gui, Ruoyu Song

School of Health Science and Engineering, University of Shanghai for Science and Technology, Shanghai 200093, China.

**Corresponding author:** Rongguo Yan.

**Declaration of conflict of interest:** None.

Received December 29, 2023; Accepted April 10, 2024; Published June 30, 2024

## Highlights

- This review introduces the basic principles and features of photoacoustic imaging technology.
- This review illustrates the application of photoacoustic imaging in the study of brain diseases.

## Abstract

Photoacoustic imaging (PAI) technology, characterized by its high resolution, minimal biological impact, and high sensitivity, has become a cornerstone in biomedical research. Its application spans various domains, showing significant promise for disease diagnosis. Currently, the majority of PAI research is conducted using animal models, with human clinical applications still in early development. This paper reviews the fundamental principles of PAI and explores its use in animal brain imaging studies. It addresses the current challenges and limitations of the technology and evaluates the potential for extending these techniques to human cerebral imaging. PAI offers substantial benefits for diagnosing neurological disorders, and its adaptation for human brain studies is crucial for advancing our understanding of neuropathogenesis, improving early disease detection, and monitoring treatment effectiveness. Continued advancements in PAI are expected to not only augment its role in neuroscience research but also establish it as a valuable tool in clinical diagnostics.

**Keywords**: Brain diseases, photoacoustic imaging, brain imaging, deep learning

## Introduction

According to 2019 statistics, brain diseases have emerged as a leading cause of death among Chinese residents, with a notable increase in their contribution to mortality and disability [1]. Stroke is the foremost cause of death and significantly impacts years of life lost. Alzheimer's disease (AD), the most common type of dementia, has escalated from 28th to 8th in disease ranking. First described by German physician Alois Alzheimer in 1906, AD is a degenerative neurological disorder characterized by memory loss, aphasia, dysarthria, impaired visuospatial skills, executive dysfunction, and changes in personality and behavior [2]. The pathogenesis of AD remains largely unclear, and diagnosis primarily depends on neuropsychological evaluations. Epidemiological projections suggest that by 2050, over 131.5 million people globally could be affected by AD. Additionally, cancers of the brain and central nervous system have moved from the 30th to the 23rd position in disease burden. Neurological disorders have also escalated in their rank as causes of disability, moving from 6th to 5th place. Consequently, brain diseases now pose the most significant health threat to the Chinese population, imposing a substantial burden on both individuals and society.

Despite a century of research, our understanding of the brain remains incomplete. Neuroscience posits that the brain is responsible for all conscious human activities, yet the exact mechanisms by which it generates consciousness and behaviors are still largely unknown due to the complex correlations between neuronal activities and these functions. While interventional electrodes allow for the observation of

**Address correspondence to: Rongguo Yan**, Department of Biomedical Engineering, School of Health Science and Engineering, University of Shanghai for Science and Technology, No. 516 Jungong Road, Yangpu, Shanghai 200093, China. E-mail: yanrongguo@usst.edu.cn.

**Table 1. Comparison of high-resolution optical imaging modalities**

| Modality | Penetration | Primary contrast |
|---|---|---|
| Confocal microscopy | ~0.5 mm | Scattering, fluorescence |
| Two-photo microscopy | ~0.5 mm | Fluorescence |
| Optical coherence tomography | ~1 mm | Scattering, polarization |
| PAI | ~3-30 mm, scalable | Absorption |

Note: PAI, photoacoustic imaging.

a limited number of neurons, they fall short of fully satisfying scientific curiosity about broader brain functions. Since 2013, several countries including the United States, China, Australia, the European Union, Japan, South Korea, and Canada have launched comprehensive "brain programs" aimed at exploring various aspects of brain function and the links between neural structure damage and disease [3-5].

Advancements in modern brain imaging techniques have significantly improved disease detection capabilities. Current imaging modalities include CT, MRI, Positron Emission Tomography (PET), Optical Imaging, Ultrasound, and Photoacoustic Imaging (PAI). However, these techniques have inherent limitations. For instance, CT, PET, and MRI often suffer from low temporal resolution, which can affect the quality of imaging. Furthermore, the equipment required for CT and MRI is not only bulky and costly but also entails high maintenance expenses and extended durations for scanning [6].

Since the 20th century, significant advancements have been made in PAI, but it was not until the early 21st century that its application in biomedical detection began to flourish. This development was largely driven by the pioneering work of Professor Wang LV's research group at the University of Washington, who explored bio-PAI techniques [7]. This research marked the onset of PAI's rise as a bio-imaging technology based on the photoacoustic effect. Currently, PAI is categorized into three main types: photoacoustic computed tomography (PACT), photoacoustic microscopy (PAM), and photoacoustic endoscopy (PAE). PACT is extensively used in human studies due to its deep tissue penetration capabilities. In contrast, PAM provides higher resolution for biomedical applications but at a reduced penetration depth. PAE, a specialized form of PAM, employs a unique scanning method to miniaturize the system for high-resolution imaging of internal organs [8].

PAI has demonstrated significant utility across various biomedical fields, including oncology, cardiovascular diseases, breast cancer, ophthalmology, and otorhinolaryngology, as well as in vivo measurements of cerebral oxygenation and microcirculation studies [9-14].

Currently, research on PAI primarily involves animal studies and has not yet fully transitioned to human clinical trials. This paper will introduce the principles of PAI technology and the application of deep learning-based PAI algorithms in brain imaging. It will also discuss the development and challenges of PAI in animal brain studies and evaluate the potential for its application in human brain imaging.

### Principles of PAI

PAI operates on the principles of the Lambert-Beer Law, a fundamental law of absorption photometry that is applicable across all forms of electromagnetic radiation and to all light-absorbing entities, including gases, solids, and liquids, as well as molecules, atoms, and ions. This law forms the foundation for quantitative spectral analysis, as depicted in equation (1).

$$A_\lambda = -\log_{10} T = kbc \tag{1}$$

Where $A_\lambda$ is the absorbance at wavelength $\lambda$, T is the transmittance, $k$ is the absorption coefficient, $b$ is the thickness of the absorbing layer, and $c$ is the concentration of the light-absorbing substance [15]. As shown in the **Table 1**, PAI exhibits greater sensitivity to light absorption compared to other optical imaging modalities [7].

The principle of the PAI technique is shown in **Figure 1**. When pulsed laser light irradiates target tissue, chromophores within the tissue absorb the energy, leading to a non-radiative transition as described by the Lambert-Beer Law. Specifically, molecular chromophores absorb photon energy, transition from the ground to an excited state, and subsequently release energy as heat. This heat causes the temperature of the target tissue to increase, inducing thermoelastic expansion that generates acoustic waves. These waves propagate as photo-

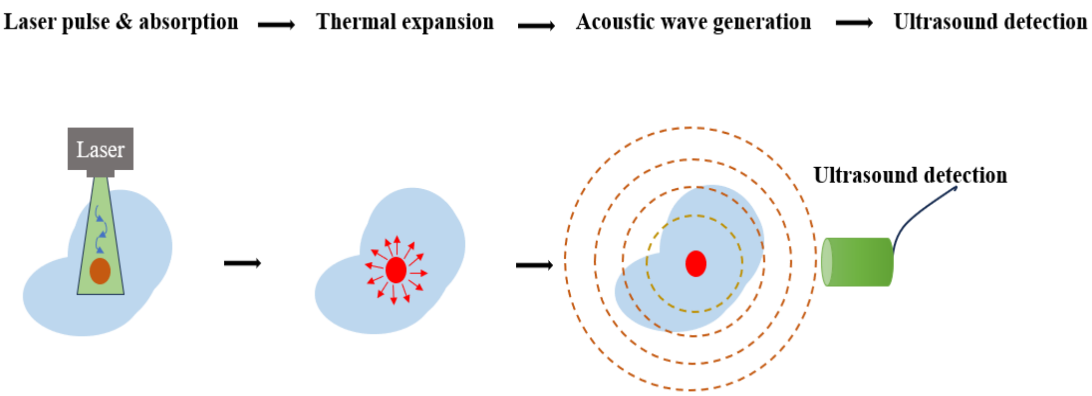


**Figure 1. Schematic diagram of photoacoustic imaging.**

acoustic signals (PAS) [16-19]. The photoacoustic effect, discovered by Alexander Graham Bell in 1880, occurs when tissues are exposed to nanosecond or picosecond pulsed lasers, producing ultrasound waves [20]. The initial sound pressure of a photoacoustic signal is calculated using the following formula:

$$P_0 = \Gamma \eta_{th} \mu_a F \quad (2)$$

Where $P_0$ is the initial pressure, $\Gamma$ is the Grüneisen parameter, $\eta_{th}$ is the photothermal conversion efficiency, $\mu_a$ is the optical absorption coefficient, and $F$ is the luminous flux. This equation illustrates that the photoacoustic signal is directly proportional to the optical absorption coefficient. A small change in the optical absorption coefficient ($\Delta\mu_a$), results in a corresponding change in the initial sound pressure ($\Delta P_0$), maintaining the ratio $\Delta P_0/ P_0=\Delta\mu_a/\mu_a$ [7]. Here the effect of $F$ on $\Delta P_0$ can be neglected.

Therefore, any fractional change in the optical absorption coefficient directly corresponds to an equivalent fractional change in the photoacoustic signal. Given that the propagation time of acoustic signals in biological tissues is substantially longer than the wavelength of light and experiences minimal attenuation, the PA signals captured by an ultrasound transducer reliably conform to Equation (3).

$$\nabla^2 P(r,t) - \frac{1}{c^2}\frac{\partial}{\partial t^2} = -P_0(r)\frac{\partial \tau(t)}{\partial t} \quad (3)$$

where $P_0(r)=\Gamma(r)A(r)$ represents the initial acoustic pressure source distribution, $c$ represents the speed of sound in the tissue, $\tau(t)$ represents the pulse width of the laser pulse, and $\Gamma(r)$ and $A(r)$ are the spatial distribution functions of the Grüneisen parameter and the optical absorption coefficients of the imaging region. The Grüneisen parameter is dimensionless and relates to the elastic modulus and specific heat capacity of the tissue.

When utilizing short-pulsed lasers with nanosecond or picosecond pulse widths as the excitation source, the duration of each pulse is significantly shorter than the thermal relaxation time of biological tissues. This temporal discrepancy ensures that heat is confined within the illuminated area, meeting the thermal confinement condition. Consequently, the absorbed material experiences an instantaneous temperature rise, leading to the generation of a shockwave with a rapid front velocity that enhances the amplitude of the resulting photoacoustic signal. Therefore, selecting a nanosecond-level pulse width for the excitation light source is critical for achieving higher signal conversion efficiency. Following this, data processing techniques are applied to the PAS to reconstruct the initial pressure distribution within the tissue and to invert the spatial distributions of optical absorption coefficients and thermal expansion characteristics, thereby providing detailed insights into the tissue's structure and function. The ultrasound detector captures the PAS induced by the photoacoustic effect in biological tissues, which underpins the application of PAI in biomedicine. The varying intensities of ultrasound generated by different biological tissues (directly proportional to the absorbed light energy) allow for the differentiation between normal and diseased tissues [8].

## Brain imaging based on deep learning

The development of PAI techniques has spurred the advancement of various PAI image reconstruction algorithms. Standard PAI reconstruction methods include Filtered Bach-Projection, Delay-And-Sum beamforming, Fourier Transform-based algorithm, and Time Reversal method. In recent years, the adoption of Deep Learning algorithms in medical image processing has grown extensively. Particularly, Convolutional Neural Network (CNN) have become the favored approach for medical image processing and analysis, including brain imaging research.

PAI reconstruction algorithms based on deep learning can be divided into two categories:

• Learning-based image optimization, where a standard reconstruction algorithm first reconstructs low-quality photoacoustic images containing artifacts from incomplete measurements. These images are then enhanced using a well-trained CNN, which removes artifacts and noise, improving image quality.

• Model-based learning and reconstruction, which incorporates a predictive photoacoustic imaging physical model into the training of CNNs for image reconstruction. The CNN serves as an iterative framework to solve the optimization problem, learning a priori knowledge for solving inverse problems from the measurement data [21]. CNN is widely used in brain imaging, with specific architectures such as U-net, Fully Dense U-net (FD U-net) being particularly popular.

Guan proposed a novel deep learning method called Pixel-Deep Learning, which first employed pixel-level interpolation controlled by the physics of photoacoustic wave propagation, followed by image reconstruction using a CNN [22]. This method was trained using a synthetic vasculature system model dataset and tested on a mouse cerebral vasculature system experiment. The results demonstrated that Pixel-Deep Learning consistently surpassed traditional post-processing reconstruction in terms of mean peak-signal-to-noise ratio and structural similarity index, achieving performance comparable to that of iterative reconstruction methods.

Using a dataset derived from the mouse cerebral microvascular system, DiSpirito et al. evaluated several CNN architectures and selected the FD U-net model for its superior performance in reconstructing undersampled PAM images [23]. This choice avoided the typical trade-off between spatial resolution and imaging speed. The FD U-net demonstrated robust capabilities in reconstructing PAM images using as little as 2% of the original pixel data, effectively reducing imaging time without compromising image quality.

Zhu et al. employed a deep learning model to enhance real-time whole-brain imaging of hemodynamics and oxygenation at microvascular resolution through ultra-fast wide-field photoacoustic microscopy [24]. The FD U-net was particularly effective in upsampling PAM images, addressing the issue of undersampling. Compared to the undersampled images, the upsampled images featured smoother vessel boundaries, reduced undersampling artifacts, and more consistent vessel intensities and contours.

Zhang et al. utilized a 2D-photoacoustic tomography (PAT) numerical model of the human brain, encompassing six tissues: scalp, skull, white matter, gray matter, blood vessels, and cerebrospinal fluid, for optical simulation [25]. The model facilitated the determination of the photoacoustic initial pressure based on the optical properties of the human brain. Subsequently, two different k-wave models were employed for cranial acoustic simulation. The photoacoustic sinusoidal maps with cranial-induced aberrations served as inputs to the U-net, while the cranial-exfoliated photoacoustic sine map acted as the supervised map for training the network. The final experimental results indicated that U-net correction effectively mitigated cranial acoustic aberrations, significantly enhancing the quality of PAT human brain images reconstructed from corrected PAS, which clearly depicted the distribution of cerebral arteries within the skull.

With the advancement of high-performance processors, big data technologies, and the proliferation of open-source databases, the application of deep learning in medical image reconstruction, particularly in PAI, has expanded significantly. Utilizing deep learning algorithms in brain studies enhances the quality of PAI, aligns with contemporary technological trends, and opens up new possibilities for the future development of PAI. However, it is crucial to recognize the limitations of deep learning algorithms, such as the need for extensive training datasets, high computational requirements, susceptibility to overfitting, and the potential loss of high-frequency detail information. These challenges highlight the ongoing need for further development in deep learning-based PAI technology.

## Progress in PAI in diagnosis of brain diseases

### *Progress in PAI for animal brain experiments*

Imaging small animals is vital in preclinical research, providing crucial physiological, pathological, and phenotypic insights with clinical relevance [26]. The necessity for animal experiments has prompted researchers to employ mouse models. Currently, many models with

**Table 2. Examples of animal brain experimental research from 2008 to 2022**

| Year | Subject | Modality | Resolution (unit: μm) |
|---|---|---|---|
| 2008 [7] | Rats | PAT | Lateral resolution: 60 |
| 2015 [29] | Rats | PAT | Lateral resolution: 243 |
| 2016 [30] | Rats | 3D-wPAT | In-plane spatial resolution: 200 |
| 2017 [26] | Rats | SIP-PACT | 125 |
| 2018 [31] | Rats | PACT | 75 |
| 2019 [32] | Rats | ORPAM | Lateral resolution: 2.25<br>axial resolution: 105 |
| 2019 [4] | Rats | MSOT | 100 |
| 2021 [33] | Monkey | p(portable)-ORPAM | Lateral resolution: 15<br>axial resolution: 120 |
| 2022 [34] | Rats | Photoacoustic neuroimaging | Axial resolution: 110 |

Note: PAT, photoacoustic tomography; wPAT, wearable photoacoustic tomography; SIP, single-impulse; PACT, photoacoustic computed tomography; ORPAM, optical resolution photoacoustic microscope; MSOT, multispectral optoacoustic tomography.

simplified geometries are unable to accurately validate PAI systems. This limitation led Grasso et al. to design and develop a stable model that closely mimics the detailed morphology of a mouse, serving as a realistic tool for PAI [27]. The creation of such mouse simulation models could diminish the need for animals in validation and standardization studies of preclinical PAI systems, thereby facilitating the transition of PAI technology into clinical research.

Several research groups around the world have conducted small animal brain imaging studies using PAI, as documented in **Table 2** [28]. The table summarizes studies from 2008 to 2022, including the year of study, experimental subjects, PAI modes, and specific resolutions achieved. Notably, PAI has significantly advanced in imaging resolution, exemplified by studies on the cerebral cortex and blood vessels of experimental rats using contrast agents at the University of Washington, USA, in 2008.

As indicated in the table, the lateral resolution of the images referenced in the literature is notably lower [32]. This reduction in resolution is attributed to the curvature of the micro-electro-mechanical-system scanner and the mismatch of refractive indices between air, glass, and water in the optical path. However, this configuration also ensures that the laser energy reaching the cerebral cortex is moderated to avoid damaging the animal tissue.

Tang et al. investigated cerebral hemodynamics and brain function in experimental rats using a novel, miniaturized 3D wearable PAT (3D-wPAT) system designed for mobile lab rats [29, 30]. This approach eliminated the potential confounding effects of anesthetics on neuronal excitability, cerebral hemodynamics, vascular reactivity, cerebral metabolism, and other physiological indices. The 3D-wPAT system featured three elevation layers with a fully functional acoustic transducer array, each consisting of 3×64 elements. Functional imaging was performed under hyperoxia conditions using multi-wavelength optical excitation (710 nm and 840 nm). The wPAT images captured from each ultrasound detection layer of the behaving rats demonstrated the capability of 3D-wPAT in imaging the brain of mobile rats. Compared to the state of the technology in 2008, spatial resolution and imaging speed have significantly improved in PAI, with 3D-wPAT requiring only 163 milliseconds to capture images, marking substantial progress in rat brain imaging [7, 29, 30].

In a related approach, Zhang also utilized behaving lab rats as experimental subjects [31]. Using a PACT system equipped with a high-frequency linear array transducer, Zhang mapped the entire brain microvascular network of rats with intact skulls to study hemodynamic activities [31]. The limited field of view of the linear array meant that only vessels perpendicular to the acoustic axis were clearly reconstructed, while vessels deviating from this axis were barely visible. To overcome this limitation, the linear array was mounted on a rotating platform centered on the rat's brain. Without altering the laser illumination, the brain was scanned comprehensively, and the images were processed to produce a full-view image. These full-view images demonstrated that the PACT system with high-frequency linear arrays could achieve high-resolution, deep functional imaging of the entire brain in mobile rats using in vivo photoacoustic computed tomography.

Chen et al. introduced a wearable, robust optical resolution photoacoustic microscope designed for freely moving rodents [32]. This device features a small, lightweight, and fast optical scanner that provides high spatiotemporal resolution, a large field of view, easy assembly, and adjustable optical focus for in vivo experiments, allowing it to image cerebral cortical activity effectively. Conversely, Qin et al. developed a fast, portable photoacoustic microscope for high-resolution in vivo imaging of the cerebral cortex in rhesus monkeys [33]. By measuring vascular diameter and functional connectivity, they analyzed the structural and functional responses of cerebral vasculature to alternating normoxic and hypoxic conditions.

Penn et al. utilized multispectral optoacoustic tomography (MSOT) to monitor neurovascular changes in a laboratory rat model of repetitive traumatic brain injury [35]. MSOT was employed to track hemoglobin content under oxygenated and deoxygenated conditions during treatment, assessing its efficacy. This study revealed MSOT's potential as a noninvasive method to monitor neurovascular changes in repetitive traumatic brain injury models, suggesting it could significantly enhance the monitoring of such injuries, which is currently costly and invasive for patients with mild conditions.

Salvas employed high-resolution ultrasound and PAI equipment (LRQA Iso9001; France Life Imaging (grant ANR-11-INBS-0006); IBISA; Leducq Foundation (RETP); I-Site Muse) to track neurovascular oxygenation and cardiac function trajectories [36]. This application of PAI in preclinical models highlighted trends in pathophysiological biomarkers that may offer new insights into the physiopathology of cardiac arrest and resuscitation.

Zhang et al. investigated PAI at three levels, i.e. brain tissue slices, isolated whole brains, and whole brains in vivo, using mice with AD pathologies [16]. The study involved APP/PS1 transgenic mice and their non-transgenic wild-type littermates. The PAI system, equipped with a 532 nm laser and a 10 ns pulse width, was used to analyze differences in brain structure and vascular networks. The distribution of photoacoustic signal amplitudes in the cerebral cortex of both mouse types was statistically analyzed. Results indicated that the amplitude distribution of PAS in the wild-type mice's cerebral cortex was narrowly ranged and smaller, whereas it was broader and higher in AD mice. These findings highlight the capacity of PAI to capture the heterogeneity of brain structure in AD, demonstrating its significant potential for monitoring structural changes and vascular characteristics in the brain during the progression of brain diseases. This technology provides deeper insights into brain science studies and the development of brain disease pathology.

The continuous exploration of PAI in animal brain imaging has led to remarkable improvements in both image penetration depth and resolution. Overall, the advances in PAI within this field offer numerous possibilities and opportunities, with the potential for further breakthroughs in bioimaging.

***Feasibility study of PAI for diagnosis of human brain diseases***

The effectiveness of biological tissue imaging is contingent upon photon penetration depth, resolution, and tissue contrast. While most deep brain functional studies currently rely on functional magnetic resonance imaging, this modality faces several limitations in achieving optimal spatiotemporal resolution and contrast. Specifically, the challenges with functional magnetic resonance imaging include: 1) relatively low spatial resolution; 2) slower temporal resolution; 3) dependency on changes in blood oxygen levels, which can be limiting; 4) susceptibility to interference from head movements.

Photon propagation in soft tissue can be segmented into four distinct regions, each defining the penetration limits for various high-resolution optical imaging modalities such as conventional planar optical microscopy, confocal microscopy, two-photon microscopy, and optical coherence tomography. As depicted in **Figure 2**, these penetration limits are set at 100 μm (aberration limit), 1 mm (diffusion limit, also referred to as the "soft limit"), 10 cm (dissipation limit), and 1 m (absorption limit) [37]. Traditional optical imaging techniques are constrained by the diffraction limit and scattering limit, which have historically impeded high-resolution imaging. However, the introduction of PAI has shown potential to surpass these longstanding barriers, offering new avenues for high-resolution imaging in the diagnosis of human brain diseases.

The penetration limits shown are order-of-magnitude approximations; wavefront-engineered penetrations are theoretical projections; this classification applies to light-scattering dominated media. Traditional optical imaging techniques face significant challenges due to strong optical scattering in tissues, which impedes high-resolution imaging beyond an optical diffusion limit of approximately 1-2 mm depth. While diffuse optical imaging methods can penetrate

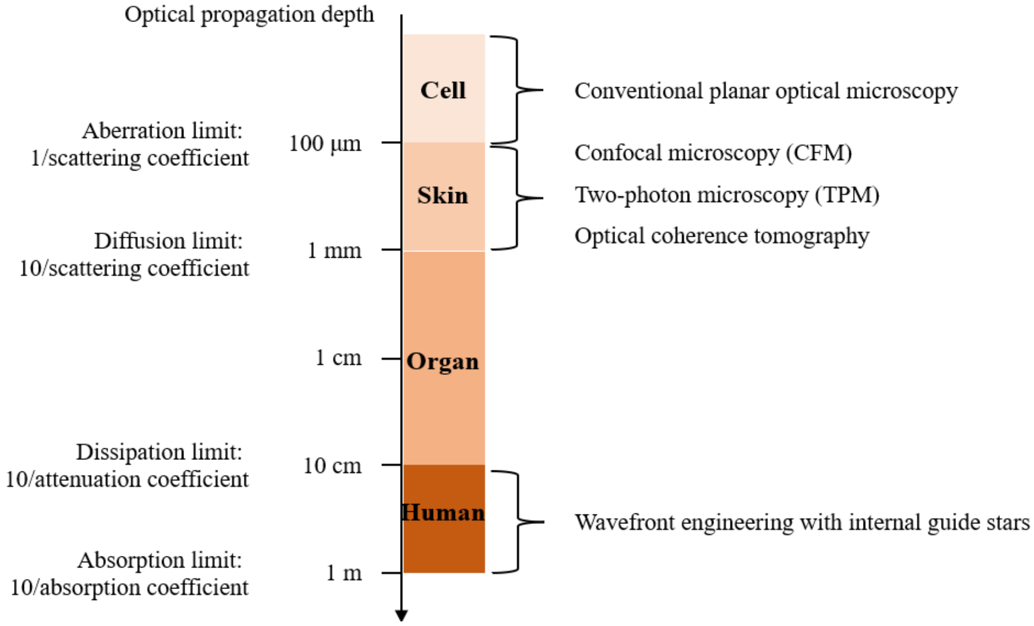


**Figure 2. The propagation of photons in soft tissue.**

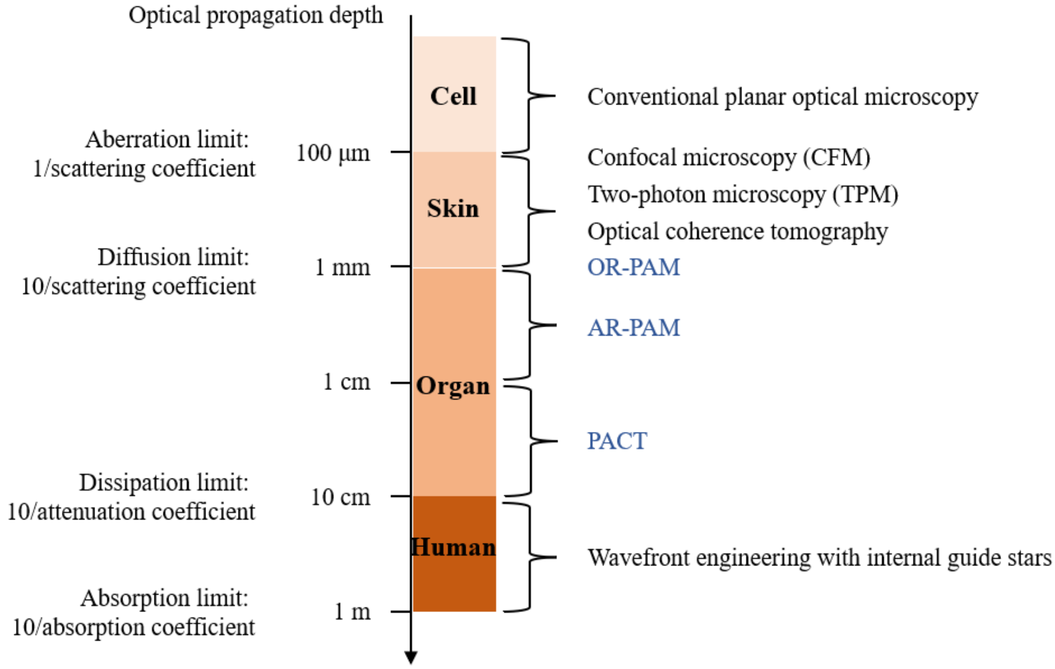


**Figure 3. Approximate positions of the three photoacoustic modes in the diagram of the penetration limit relationship.** OR-PAM, optical resolution photoacoustic microscope; AR-PAM, acoustic resolution photoacoustic microscopy; PACT, photoacoustic computed tomography.

to depths of several centimeters, their resolution remains low, approximately one-third of the penetration depth [26].

PAI, a hybrid imaging modality, merges the high contrast and spectral recognition capabilities of optical imaging with the deep penetration and high resolution of ultrasound imaging. This modality is poised to surmount the limitations of traditional optical imaging techniques by providing high-resolution images at significant depths.

Compared with conventional medical imaging technologies, PAI offers distinct advantages:

• It achieves selective excitation of specific spectral tissues, capturing both structural and functional imaging features, thus introducing a novel imaging method distinct from traditional techniques.

• By combining the benefits of optical and acoustic imaging, it overcomes the “soft limit” of depth in high-resolution optical imaging, such as laser confocal microscopy, two-photon excitation microscopy, and optical coherence tomography, while simultaneously achieving higher resolution for molecular imaging.

• PAI is a non-invasive, non-ionizing, and damage-free technology [38].

**Figure 3** illustrates the approximate positions of three typical PAI modalities (OR-PAM, AR-PAM, and PACT)—in relation to the penetration limit. The spatial resolution of PAT varies with imaging depth, transitioning from the quasi-ballistic state (typically ≤1 mm in tissue) to the diffuse state (typically ≥10 mm in tissue), and reaching up to the dissipation limit (approximately 10 cm in tissue). Reducing the imaging depth in PAT can effectively enhance its spatial resolution, offering a strategic approach to improving image quality.

As early as 2013, Gong provided an overview of biomedical PAI technology, which has since become one of the fastest-growing technologies in the field due to advances in laser and ultrasound detection technologies [39]. In terms of laser technology, to ensure higher signal conversion efficiency, the pulse width of the excitation light source is typically selected at the nanosecond level. By choosing specific wavelengths of light, targeted absorption can be identified based on differences in absorption coefficients. For instance, deoxy-hemoglobin (HbR) is more sensitive at 710 nm, while oxy-hemoglobin (HbO) is more sensitive at 840 nm. Using these wavelengths, Tang et al. conducted three-layer ultrasound detection for brain imaging in behaving rats [29].

In terms of ultrasound detection, the choice of detection method significantly affects imaging quality, depending on the intensity of the generated sound waves. For example, current PACT systems primarily use arrayed ultrasound transducers. These transducers can be categorized into planar, cylindrical, and spherical arrays. Planar array transducers, often integrated with the light source, are low-cost and straightforward to construct, making them prevalent in PACT applications. Conversely, cylindrical, and spherical array transducers, which are typically customized, are more costly and bulky but are necessary for specific imaging requirements, such as small animal imaging and functional imaging of brain structures. Matching the ultrasound transducer’s spectrum with the photoacoustic signal’s spectrum, utilizing higher central frequencies, and employing wider bandwidths can all enhance imaging quality. Therefore, it is crucial to consider various factors based on actual imaging needs to select the appropriate ultrasound transducers and detection methods for high-quality PAI.

Understanding how our brain functions represents a significant challenge in the field of PAI. Probing the brain is crucial not only for unraveling profound scientific mysteries but also for advancing our understanding and treatment of neurological disorders, such as AD and Parkinson’s disease [2]. In summary, PAI offers several feasible capabilities:

• PAI transcends the fundamental depth limitations of current high-resolution optical imaging modalities. It holds significant promise for human brain imaging due to its high spatial resolution, tissue quantification, and deep imaging capabilities [36].

• The relationship between imaging depth and spatial resolution is approximately constant, maintaining proportionality as both dimensions are scaled.

• PAI exhibits high sensitivity to light absorption, enabling precise detection of changes within tissues.

• PAI facilitates functional imaging by exploiting physiologically specific endogenous optical absorption contrasts.

• PAI has the potential for real-time imaging applications, enhancing its utility in dynamic clinical environments.

• PAI is safe for human use, making it a promising tool for clinical applications.

## Conclusion

After decades of development, PAI technology has diversified, merging the strengths of pure optical imaging and ultrasonography. It plays a pivotal role in studying various brain tissues, notable for its high resolution, minimal biological damage, and high sensitivity, showcasing its potential for biomedical applications. However, current research on PAI for brain imaging is predominantly confined to small animal models. The intense scattering and attenuation of ultrasonic signals by human cranial bones lead to weakened PAS and expanded bandwidth, consequently impairing imaging depth and spatial resolution. The primary challenges facing PAI in brain imaging include: 1) limited penetration depth; 2) the trade-off between resolution and depth; 3) dependency on tissue optical properties; 4) interference from cranial bones; 5) hurdles in clinical applications.

In conclusion, PAI offers significant advantages for diagnosing brain diseases. Nevertheless, substantial challenges remain for its widespread clinical application in humans, particularly in understanding the pathogenesis of brain diseases, achieving early diagnosis, and monitoring treatment effectiveness. With ongoing advancements and broader adoption of PAI technology, its potential in brain disease research and other medical fields is promising, positioning it as an important tool for clinical diagnosis.

**Author Contributions:** Tingting Shi performed the data analyses and wrote the manuscript; Tingting Shi, Rongguo Yan, Xinrui Gui, and Ruoyu Song contributed significantly to analysis and manuscript preparation.

## References

[1] Zhou M, Wang H, Zeng X, et al. Mortality, morbidity, and risk factors in China and its provinces, 1990-2017: a systematic analysis for the Global Burden of Disease Study 2017. Lancet 2019;394:1145-1158.
[2] Huang YX, Zhou FF, Zhou T, et al. Application of multiphoton microscopic imaging in the research on brain disease. Prog Biochem Biophys 2019;46:952-965.
[3] Rommelfanger KS, Jeong SJ, Ema A, et al. Neuroethics Questions to Guide Ethical Research in the International Brain Initiatives. Neuron 2018;100:19-36.
[4] Olefir I, Ghazaryan A, Yang H, et al. Spatial and Spectral Mapping and Decomposition of Neural Dynamics and Organization of the Mouse Brain with Multispectral Optoacoustic Tomography. Cell Rep 2019;26:2833-2846.e3.
[5] Chen H, Mirg S, Gaddale P, et al. Dissecting Multiparametric Cerebral Hemodynamics using Integrated Ultrafast Ultrasound and Multispectral Photoacoustic Imaging (Preprint). bioRxiv 2023.
[6] Chandra R, Zhou H, Balasingham I, et al. On the Opportunities and Challenges in Microwave Medical Sensing and Imaging. IEEE Trans Biomed Eng 2015;62:1667-1682.
[7] Wang LV. Tutorial on Photoacoustic Microscopy and Computed Tomography. IEEE J Sel Top Quantum Electron 2008;14:171-179.
[8] Shen XW, Wu HP, Dong L. Recent advances of photoacoustic imaging technology in biomedicine (Invited). Acta Photonica Sin 2023;52:81-99.
[9] Nasri D, Manwar R, Kaushik A, et al. Photoacoustic imaging for investigating tumor hypoxia: a strategic assessment. Theranostics 2023;13:3346-3367.
[10] Khan F, Naeem K, Khalid A, et al. Photoacoustic imaging for characterization of radiofrequency ablated cardiac tissues. Lasers Med Sci 2023;38:61.
[11] Yu C, Kong L, Tian J, et al. Photoacoustic imaging-guided triple-responsive nanoparticles with tumor hypoxia relief for improving chemotherapy/photothermal/photodynamic synergistic therapy against breast cancer. Biomed Pharmacother 2023;164:114928.
[12] Samanta D, Paul S, Paramanick A, et al. High-resolution imaging of the whole eye with photoacoustic microscopy. Opt Lett 2023;48:3443-3446.
[13] Manwar R, McGuire LS, Islam MT, et al. Transfontanelle photoacoustic imaging for in-vivo cerebral oxygenation measurement. Sci Rep 2022;12:15394.
[14] Mirg S, Turner KL, Chen H, et al. Photoacoustic imaging for microcirculation. Microcirculation 2022;29:e12776.
[15] Zhang JH, Zhang W, Shi JQ, et al. Selection and application of spectral data preprocessing strategy. Acta Metrol Sin 2023;44:1284-1292.
[16] Zhang ZH, Wang EQ, Shi YJ. Applications of photoacoustic technology in brain tissue imaging (invited). Infrared Laser Eng 2022;51:90-96.
[17] Li YX, Hu CQ, Ma LF, et al. Research Progress in Intelligent and Precise Optical Diagnosis and Treatment Technology. Chin J Lasers 2021;48:282-302.
[18] Beard P. Biomedical photoacoustic imaging. Interface Focus 2011;1:602-631.
[19] Mu G, Zhang ZH, Shi YJ. Photoacoustic imaging technology in biomedical imaging. Chin J Lasers 2022;49:133-151.
[20] Bell AG. On the production and reproduction of sound by light. Am J Sci 1880;s3-s20:305-324.
[21] Sun Z, Wang XY. Application of deep learning in photoacoustic imaging. Comput Sci 2020;47:148-152.
[22] Guan S, Khan AA, Sikdar S, et al. Limited-View and Sparse Photoacoustic Tomography for Neuroimaging with Deep Learning. Sci Rep 2020;10:8510.
[23] DiSpirito A, Li D, Vu T, et al. Reconstructing Undersampled Photoacoustic Microscopy Images Using Deep Learning. IEEE Trans Med Imaging 2021;40:562-570.
[24] Zhu X, Huang Q, DiSpirito A, et al. Real-time whole-brain imaging of hemodynamics and

oxygenation at micro-vessel resolution with ultrafast wide-field photoacoustic microscopy. Light Sci Appl 2022;11:138.

[25] Zhang F, Zhang J, Shen Y, et al. Photoacoustic digital brain and deep-learning-assisted image reconstruction. Photoacoustics 2023;31:100517.

[26] Li L, Zhu L, Ma C, et al. Single-impulse Panoramic Photoacoustic Computed Tomography of Small-animal Whole-body Dynamics at High Spatiotemporal Resolution. Nat Biomed Eng 2017;1:0071.

[27] Grasso V, Raymond JL, Willumeit-Römer R, et al. Development of a morphologically realistic mouse phantom for pre-clinical photoacoustic imaging. Med Phys 2023;50:5757-5771.

[28] Su L, Li TM. Progress of biophotonics technology in brain function research. J Univ Electron Sci Technol China 2023;52:296-305.

[29] Tang J, Xi L, Zhou J, et al. Noninvasive high-speed photoacoustic tomography of cerebral hemodynamics in awake-moving rats. J Cereb Blood Flow Metab 2015;35:1224-1232.

[30] Tang J, Coleman JE, Dai X, et al. Wearable 3-D Photoacoustic Tomography for Functional Brain Imaging in Behaving Rats. Sci Rep 2016;6:25470.

[31] Zhang P, Li L, Lin L, et al. High-resolution deep functional imaging of the whole mouse brain by photoacoustic computed tomography in vivo. J Biophotonics 2018;11:10.

[32] Chen Q, Xie H, Xi L. Wearable optical resolution photoacoustic microscopy. J Biophotonics 2019;12:e201900066.

[33] Qin W, Gan Q, Yang L, et al. High-resolution in vivo imaging of rhesus cerebral cortex with ultrafast portable photoacoustic microscopy. Neuroimage 2021;238:118260.

[34] Jin T, Qi W, Liang X, et al. Photoacoustic Imaging of Brain Functions: Wide Field-of-View Functional Imaging with High Spatiotemporal Resolution. Laser Photonics Rev 2023;17:2300067.

[35] Penn C, Katnik C, Cuevas J, et al. Multispectral optoacoustic tomography (MSOT): Monitoring neurovascular changes in a mouse repetitive traumatic brain injury model. J Neurosci Methods 2023;393:109876.

[36] Salvas JP, Leyba KA, Schepers LE, et al. Neurovascular Hypoxia Trajectories Assessed by Photoacoustic Imaging in a Murine Model of Cardiac Arrest and Resuscitation. IEEE Trans Ultrason Ferroelectr Freq Control 2023;70:1661-1670.

[37] Wang LV, Yao J. A practical guide to photoacoustic tomography in the life sciences. Nat Methods 2016;13:627-638.

[38] Ceng LZ, Yang SH, Xing D. Progress on photoacoustic imaging and its biomedical application. J South China Norm Univ (Nat Sci Ed) 2016;48:9-15.

[39] Gong XJ, Meng J, Chen JH, et al. Biomedical photoacoustic tomography technology and its clinical applications. J Integr Technol 2013;2:53-59.

Progress in Medical Devices
eISSN: 2957-5478

Review Article https://doi.org/10.61189/758818obsmms

# Advancements in irreversible electroporation ablation technology for treating atrial fibrillation

Binyu Wang, Tiantian Hu, Jiuzhou Zhao, Jincheng Xu, Banghong Chen, Yicheng Liu, Yu Zhou

School of Health Science and Engineering, University of Shanghai for Science and Technology, Shanghai 200093, China.

**Corresponding author:** Yu Zhou.

**Declaration of conflict of interest:** None.

Received January 17 2024; Accepted February 7, 2024; Published June 30, 2024

## Highlights

- Pulsed field ablation (PFA) demonstrates superior efficacy atrial fibrillation than traditional methods.
- Enhanced safety profile of PFA reduces complications in adjacent tissue damage.
- Optimized outcomes depends on key PFA parameters such as voltage, pulse width, and frequency.

## Abstract

Pulsed field ablation (PFA), an emerging treatment method for atrial fibrillation, has demonstrated significant potential in arrhythmia therapy. PFA employs high-intensity, short-duration electric fields to induce irreversible electroporation in myocardial cells, disrupting abnormal cardiac rhythms, and restoring normal heart function. This technique exhibits high success rates and low recurrence rates in animal studies and early clinical trials, offering advantages over traditional methods by reducing damage to adjacent structures such as the esophagus, phrenic nerve, and pulmonary veins. This review examines PFA's application mechanisms, benefits, key operational parameters and the design and safety of related ablation devices. It emphasizes PFA's potential to enhance both the efficacy and safety of atrial fibrillation treatment and explores future research directions and technological developments.

**Keywords**: Irreversible electroporation, pulsed field ablation, atrial fibrillation treatment, ablation devices

## Introduction

Irreversible electroporation (IRE) involves the formation of irreversible micropores in the cell plasma membrane when exposed to a strong electric field [1, 2]. These pores, termed irreversible electropores, induce cell apoptosis due to osmotic imbalance once their quantity on the cell membrane reaches a critical threshold. As an innovative medical intervention, IRE has shown tremendous potential in treating arrhythmias, especially atrial fibrillation (AF).

AF is a common cardiac disorder, primarily treated clinically through catheter ablation techniques [3]. Traditional catheter ablation methods, particularly radiofrequency ablation (RFA) and cryoballoon ablation, function by damaging abnormal cardiac cells through temperature modulation [4, 5]. Although effective in some cases, these methods depend on efficient heat transfer from the catheter to the target tissue, necessitating substantial contact between the catheter and cardiac tissue. More importantly, the potential adverse effects of thermal action on cardiac cells and surrounding sensitive tissues, such as the esophagus, veins, and phrenic nerve can lead to adjacent tissue damage, complicating postoperative recovery and increasing risks.

To overcome these limitations, scientists have introduced treatment methods based on IRE technology. Unlike traditional thermal ablation methods, IRE-based treatments do not rely on thermal effects to eliminate cells, thereby significantly shortening treatment duration and accelerating the process [6]. Additionally, this

**Address correspondence to: Yu Zhou,** School of Health Science and Engineering, University of Shanghai for Science and Technology, No.516 Jungong Road, Changbai New Village Street, Yangpu District, Shanghai 200093, China. Tel: 18021042556. E-mail: zhouyu@usst.edu.cn.

approach exploits the lower electric field tolerance threshold of myocardial cells compared to vascular tissues, allowing for more precise targeting of myocardial cells without damaging surrounding vascular structures [7-9]. This selectivity is crucial for protecting non-target tissues and provides a safer and more effective AF treatment option with the clinical application of IRE technology.

### Technical advantages of IRE tissue selectivity

Pulsed field ablation (PFA) technology plays a crucial role in the selective damage cardiac tissues, while effectively avoiding damage to adjacent myocardial tissues such as the esophagus and phrenic nerve. This technology achieves electroporation effects by releasing high-intensity electric fields within a microsecond pulse width. When the electric field strength surpasses the irreversible damage threshold of specific cells, it can selectively affect these cells [9]. Studies have shown that the IRE damage threshold of myocardial cells is lower than that of adjacent esophageal and phrenic nerve tissues [7, 8]. Therefore, precise parameter adjustments make it possible to damage myocardial cells specifically while avoiding similar effects on adjacent tissues.

Initially verified through animal experiments by Koruth et al., this theory involved placing a mesh-like ablation catheter and a RFA catheter in the inferior vena cava, with the esophagus fixed behind it, using a particular device [10]. Post-ablation observations revealed that pulsed ablation technology did not cause damage to the esophagus, while RFA led to esophageal fistulas or ulcers [10]. Notably, although the smaller diameter of the mesh structure used in this study than the standard clinical size, resulting in a stronger electric field at the same voltage, the animal experiment results still confirmed the effectiveness of the tissue-selective damage mechanism.

Further clinical data supported these findings. In postoperative evaluations, certain patients showed no esophageal damage as assessed by enhanced magnetic resonance imaging examinations [11]. Besides, clinical trials identified two cases of persistent diaphragmatic nerve damage in the radiofrequency/cryoablation group, while no similar cases were recorded in the PFA group [12].

### Ablation safety

IRE incites a markedly reduced inflammatory response compared to radiofrequency/cryoablation, thereby diminishing the risk of pulmonary vein constriction. Unlike radiofrequency/cryoablation, which utilizes thermal conduction to inflict tissue damage, typically leading to coagulative necrosis, inflammatory responses, and fibrosis. PFA operates via an electroporation mechanism, leading cells to undergo apoptosis rather than necrosis, thus avoiding microvascular occlusion and intramural hemorrhage. This difference in mechanism is crucial for tissue recovery. Perioperative MRI detection indicates that myocardial areas treated with PFA demonstrate the potential for tissue tension recovery, a phenomenon not observed with RFA [13]. Research by Reddy et al., comparing the effects of the two techniques on pulmonary vein diameter, found PFA to be as efficacious as thermal ablation in maintaining vein diameter [12].

### Impact of different pulse parameters on the treatment of AF

Understanding the operational parameters of IRE is vital for optimizing its application in treating AF. Pulse frequency, width, and duration are pivotal in determining treatment efficacy, influencing electric field interaction with cells and the extent of cell apoptosis.

Baena et al. demonstrates that apoptosis induction by pulsed electric fields (PEFs) correlates with field strength, pulse width, and duration [14]. Applying electric fields from 250 to 1000 V/cm to human myocardial cells, significant electroporation and cell death occurred at 750 V/cm, with a pulse width of 100 μs, and of 3 ms. Effects were similar at a reduced field strength of 250 V/cm with a pulse duration extended to 60 ms. Additionally, short pulses of 2 and 5 μs at field strengths above 1000 V/cm significantly induced apoptosis. Prado et al. noted that induce cell death with shorter pulse necessitates higher electric field strengths [15].

Jiang et al. suggested that the stochastic nature of IRE, indicating that not all cells undergo apoptosis under high electric field conditions if the pulse number or duration is insufficient [6]. Cardiac cell survival drops below 90% at field strengths above 750 V/cm. However, almost complete cell death (over 90%) is achievable at strengths above 1250 V/cm with adequate pulse numbers or duration. In the 750 to 1250 V/cm range, cells might be damaged without immediate death. Interestingly, increasing pulse numbers or duration does not enhance cell damage at low electric field strengths (below 500 V/cm), contrary to Rubinsky et

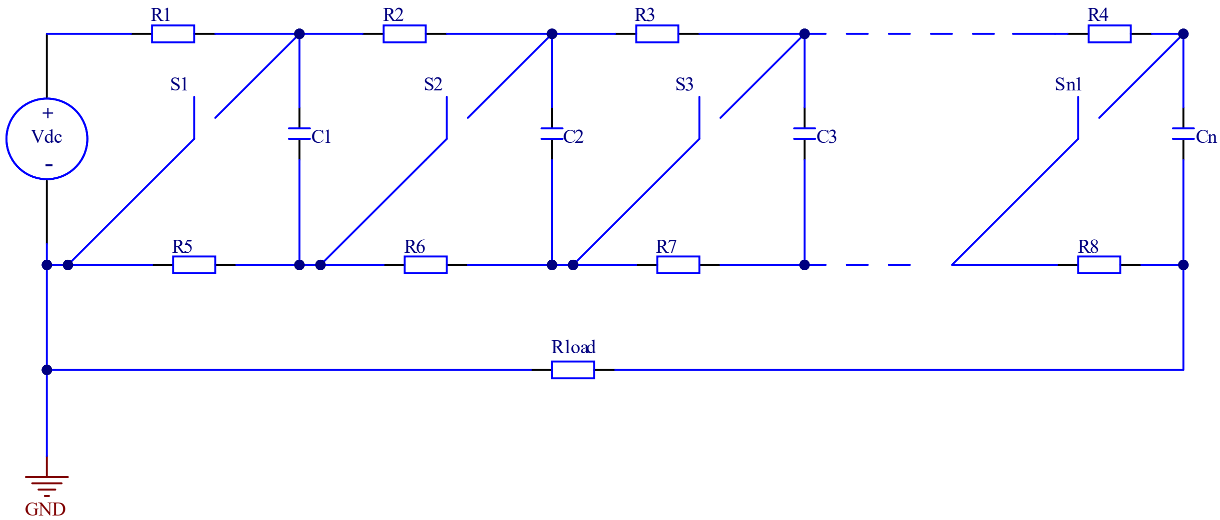

**Figure 1. Basic topology of a Marx generator.** Vdc, voltage direct current; GND, ground.

al., who achieved 100% cell death at 125 V/cm with significantly more pulses (up to 3840 compared to Jiang et al.'s maximum of 90) [16, 17]. Thus, investigating complete IRE-induced cell death with sufficient pulse numbers at low electric field strengths (below 500 V/cm) and its clinical relevance merits further research.

Miklovic et al. demonstrated that under constant electric field strength, pulse trains with wider pulse widths significantly enhance tissue ablation efficacy [18]. Specifically, a 50 μs pulse train produced an ablation volume 7.2 times larger than a 1 μs pulse train. However, they noted that extended pulse durations could induce severe muscle contractions, potentially leading to arrhythmias. An oversight in their report was the omission of pulse frequency, a critical parameter in IRE effectiveness. A study investigated the impact of various pulse frequencies on IRE treatment outcomes, employing pulse energies from 250 kHz to 2 MHz to [19]. The results indicated that, with all other parameters constant, a frequency of 250 kHz was most effective, with diminishing efficacy at higher frequencies. This trend may be attributed to the increase in high-frequency components which, according to bioimpedance theory, allow displacement currents at higher frequencies to penetrate cell membranes directly [20]. Thus, high-frequency pulses tend to affect internal cellular structures, like the nucleus and organelles, rather than the cell membrane's surface.

## IRE ablation devices

### *Pulse power supply unit*

The pulse power supply unit's primary function is to energize the pulse forming unit, a critical aspect influencing the entire system's performance. This involves determining the energy storage module's charging speed in the pulse forming unit, which affects the system's maximum pulse frequency.

DC-DC high-voltage generation, pivotal in power conversion, offers notable stability in switching frequency and constant charging current. The LLC resonant circuit, used in high-voltage DC-DC converters, leverages inductance and capacitance resonance for, reducing switching losses and improving energy conversion efficiency. Azura et al. developed a DC-DC converter using LLC resonance, featuring a full-bridge inverter, an LLC resonant tank, a high-voltage transformer, and a full-bridge rectifier [21]. This converter, achieving ZVS through leakage energy and LLC resonance, showcased superior efficiency with a 300 V input to 3.5 kV/0.35A output, confirmed by design examples and simulations.

### *Pulse forming unit*

The development of IRE ablation devices critically depends on the pulse forming unit, which utilizes high-voltage pulse generators, predominantly of the capacitor discharge type. This approach employs capacitors as energy storage, which are charged and then discharged through a switch to deliver high-voltage pulses. The Marx generators and H-bridge circuits are prevalent in capacitor discharge high-voltage pulse generation.

A Marx generator, with its simple structure and modest input power requirements, charges capacitors $C_1$-$C_n$ in parallel and t discharges them in series to generate high-voltage pulses (**Figure 1**). Its ability to generate high voltages through cascading makes it a staple in pulse signal design. Advancements in switch technology have

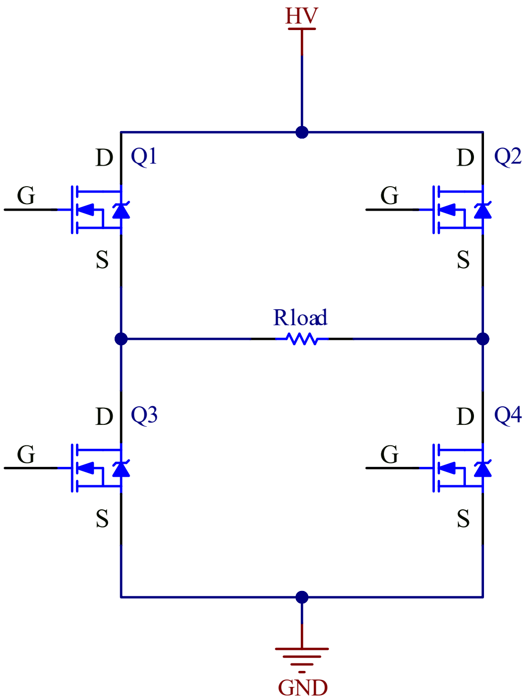


**Figure 2. Basic topology of an H-bridge circuit.** HV, high voltage; GND, ground.

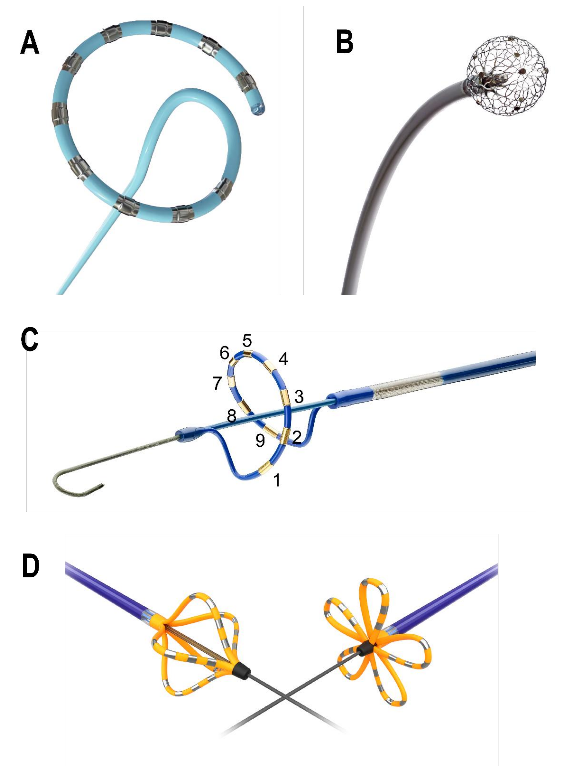


**Figure 3. Different Types of PFA Electrodes.** (A) VARIPULSE ablation electrode; (B) Sphere-9 catheter; (C) pulse select ablation electrode; (D) FARAWAVE ablation electrode. The subfigures A, B, C, D were cited from [24], [26], [28], [31], respectively. PFA, pulsed field ablation.

made solid-state switches, such as MOSFETs, vital due to their compactness, controllability, and high repetition capabilities. Yao et al. replaced traditional spark gaps with MOSFETs in a Marx generator, achieving pulse durations in the hundreds of nanoseconds, adjustable pulse widths from 200 to 1000 ns, rise times of 35 ns, and a frequency range of 1 to 1000 Hz, illustrating the potential for precise and efficient IRE ablation [22].

The H-bridge circuit, essential for generating positive and negative pulses, consists of four switching devices arranged in an "H" configuration (**Figure 2**). This setup enables control over the current flow direction by alternating the activation of these devices. Jiang et al. introduced a novel bipolar modular multilevel generator based on an H-bridge design, comprising a full-bridge module and multiple half-bridge modules [17]. This generator can produce up to 2000 V, 2 μs nine-level step pulse waves, and adjustable square waves with 1-10 μs pulse widths. Furthermore, Pirc et al. developed a device capable of emitting a maximum voltage of 4 kV and a maximum current of 131 A, with pulse durations as brief as 200 ns and a repetition rate up to 2 MHz [23]. This device produces asymmetric bipolar pulses, allowing independent adjustment of both pulse duration and amplitude.

***IRE ablation devices: electrode needles***

In the development of IRE ablation devices, the design of ablation electrode needles is equally crucial. The effectiveness and safety of the ablation treatment depend directly on these needles, as they deliver the PEF generated by the pulse forming unit to myocardial cells.

The VARIPULSE ablation electrode (Biosense Webster, California, USA), featuring a 7.5F diameter, incorporates 10 ring electrodes spaced 5 millimeters apart, each 2 millimeters in length [24]. This configuration allows for an adjustable diameter disk, varying from 25 to 35 millimeters, as seen in **Figure 3A**. This figure was cited from [24]. Such a design adapts to different pulmonary vein openings, offering flexibility in clinical applications. Additionally, the catheter also boasts bidirectional bending capabilities—up to 180° in one direction and 90° in the other—enhancing ease of use and precision in engaging with all pulmonary veins. Yavin et al. assessed the feasibility of using the VARIPULSE ablation electrode to create block lines from the superior vena cava to the inferior vena cava, examining its effects on cardiac lesions and esophageal and phrenic nerve tissues [25]. This comprehensive study included an atrial line model assessment and detailed analysis of PFA's impact on the esophagus and phrenic nerve. Histopathological and statistical analyses, conducted with Stata/SE software, confirmed that PFA could effectively establish continuous and transmural block lines in the atrium without causing significant harm to the esophagus and phrenic nerve.

The Sphere-9 catheter, also known as the Lattice-tip catheter (Affera, Nevada, USA) features an expandable spherical mesh tip, offering an effective area ten times larger than traditional 3.5 mm electrodes [26]. Its design enhances higher energy output while mitigating the risk of tissue overheating. The spherical ablation electrode is equipped with perfusion micro-holes and a central reference electrode for both measurement and ablation purposes, as seen in **Figure 3B**. This figure was cited from [26]. Capable of supporting both radiofrequency and PEF energy modes. In the study by Reddy et al. on 76 patients confirmed the system's safety and efficacy for pulmonary vein isolation and linear ablation tasks, with RFA/PFA and PFA/PFA strategies demonstrating solid acute efficacy and safety profiles [27].

The PulseSelect ablation electrode (Medtronic, Minneapolis, USA) features a catheter head with extend able electrodes forming a "disc-like" shape, 25 mm in diameter, where odd-numbered electrodes act as positive and even-numbered as negative [28]. The design, which includes a 20° forward tilt for ease of use, as shown in **Figure 3C**. This figure was cited from [28]. Stewart et al. carried out ablation experiments on pig hearts, showing that PFA effectively reduced local electrogram amplitudes and produced durable effects in AF treatment, surpassing RFA in lesion healing smoothness, without affecting surrounding tissues [29]. In a clinical study by Verma et al., all 38 patients achieved intraoperative PVI safely with the PFA system [30].

The FARAWAVE ablation electrode, also known as the petal-type ablation electrode (FARAPULSE, Menlo Park, USA), uses a 12 F diameter design with 5 petal-shaped semi-rings, each containing 4 electrodes, presenting a basket-like structure when not fully expanded and a petal shape upon expansion., as shown in **Figure 3D**. This figure was cited from [31]. Reddy et al. evaluated its use in PFA for PVI and treating atrial flutter in 121 patients, highlighting PFA's rapid PVI achievement and low safety event rate (1.2%), with no observed pulmonary vein stenosis or damage to adjacent structures [32, 33].

## Emerging insights on PFA in AF treatment

Reddy et al. pioneered the application of PFA in treating atrial fibrillation in humans, detailing a study involving 22 patients [34]. Fifteen patients received endocardial PFA under general anesthesia, utilizing a petal-style electrode catheter guided to the pulmonary vein ostia with intracardiac ultrasound and fluoroscopy. This initial foray reported a 100% success rate in pulmonary vein isolation (PVI) via the endocardial route, with an 87.5% success rate for epicardial route ablations, without adverse events like malignant arrhythmias or ventricular dysfunction. Notably, right-side nerve function remained intact post-ablation.

A subsequent study of 81 patients, employing bipolar voltages between 1800 and 2000 V and unipolar voltages between 900 and 1000 V, recorded no acute adverse events, showcasing PFA's swift ablation and minimal fluoroscopy time. Three-month follow-up electrophysiological exams confirmed a 100% success rate in achieving circumferential PVI, with no significant damage to nerves or the esophagus, underscoring PFA's durability and safety [33].

More recently, Reddy et al. explored PFA's long-term efficacy in a trial with 121 patients, revealing a one-year atrial arrhythmia recurrence rate between 78.5%±3.8% and 84.5%±5.4% for the optimized PFA energy group, indicating effective long-term PVI and AF treatment [32].

Another innovative study utilized the Lattice-tip catheter for complex ablation treatments in 76 patients, incorporating both RFA and PFA [27]. Preliminary findings suggested enhanced treatment efficacy and reduced fluoroscopy time, with no perioperative device-related complications. Importantly, no thermal injury to the esophagus was observed, affirming PFA's safety.

While initial findings are promising, further research and long-term follow-up are essential to fully assess the clinical effectiveness and patient outcomes of PFA in treating AF. Future studies are critical for evaluating the sustained efficacy and therapeutic benefits of this combined treatment strategy, providing deeper insights into arrhythmia treatment.

## Conclusion

PFA represents a burgeoning technology in the treatment of AF, showing considerable promise. Its distinct advantage lies in its targeted disruption of atrial myocardial cells, significantly reducing the risk of pulmonary vein stenosis and sparing adjacent structures such as the esophagus, autonomic nervous system, and coronary arteries. Both animal studies and early clinical trials have attested to its viability and safety. Yet, the nascent state of current clinical research, characterized by limited sample sizes and brief follow-up durations, necessitates further investigation to corroborate and refine PFA's efficacy.

The success of PFA is contingent upon a multitude of factors, including voltage strength, pulse width, frequency, waveform, field intensity, and the pulse's vector direction, all of which influence the procedure's reach and impact. Therefore, identifying the optimal parameter configuration for specific clinical scenarios remains an area ripe for exploration. As medical device technology progresses, future evidence-based research is anticipated to bolster PFA's role in cardiac ablation, offering a more accurate and safer option for cardiac arrhythmia treatment.

**Author Contributions:** Binyu Wang collected and organized data, wrote the paper, revised the manuscript, and created charts and diagrams. Tiantian Hu contributed to writing the paper and refined the content. Jiuzhou Zhao reviewed literature, gathered information, and created charts and diagrams. Jincheng Xu proofread the manuscript. Banghong Chen proofread the manuscript. Yicheng Liu researched and compared existing instruments in the market. Yu Zhou supervising professor, provided writing guidance, and advised on the paper's composition.

## References


[1] Yao CG, Sun CX, Mi Y, et al. Experimental studies on Killing and inhibiting effects of steep pulsed electric field (SPEF) to target cancer cell and solid tumor. IEEE Trans Plasma Sci 2004;32(4):1626-1633.

[2] Kotnik T, Kramar P, Pucihar G, et al. Cell membrane electroporation- Part 1: The phenomenon. IEEE Electr Insul Mag 2012;28(5):14-23.

[3] Pappone C, Santinelli V. Atrial Fibrillation Ablation. Rev Esp Cardiol (Engl Ed) 2012;65(6):560-569.

[4] Cosedis Nielsen J, Johannessen A, Raatikainen P, et al. Radiofrequency Ablation as Initial Therapy in Paroxysmal Atrial Fibrillation. N Engl J Med 2012;367:1587-1595.

[5] Kuck KH, Brugada J, Fürnkranz A, et al. Cryoballoon or Radiofrequency Ablation for Paroxysmal Atrial Fibrillation. N Engl J Med 2016;374:2235-2245.

[6] Jiang C, Davalos RV, Bischof JC. A review of basic to clinical studies of irreversible electroporation therapy. IEEE Trans Biomed Eng 2015;62:4-20.

[7] Cicek F, Coskun C, Baldan I, et al. Pre-application of pulsed magnetic field protects oxidative stress-induced apoptosis of vascular smooth muscle cells. Int J Radiat Res 2022;20:277-282.

[8] Sauer H, Rahimi G, Hescheler J, et al. Effects of electrical fields on cardiomyocyte differentiation of embryonic stem cells. J Cell Biochem 1999;75:710-723.

[9] Hunter DW, Kostecki G, Fish JM, et al. In Vitro Cell Selectivity of Reversible and Irreversible: Electroporation in Cardiac Tissue. Circ Arrhythm Electrophysiol 2021;14:e008817.

[10] Koruth JS, Kuroki K, Kawamura I, et al. Pulsed Field Ablation Versus Radiofrequency Ablation: Esophageal Injury in a Novel Porcine Model. Circ Arrhythm Electrophysiol 2020;13:e008303.

[11] Grosse Meininghaus D, Freund R, Koerber B, et al. Pulsed-field ablation does not induce esophageal and periesophageal injury-A new esophageal safety paradigm in catheter ablation of atrial fibrillation. J Cardiovasc Electrophysiol 2024;35:86-93.

[12] Reddy VY, Gerstenfeld EP, Natale A, et al. Pulsed Field or Conventional Thermal Ablation for Paroxysmal Atrial Fibrillation. N Engl J Med 2023;389:1660-1671.

[13] Nakatani Y, Sridi-Cheniti S, Cheniti G, et al. Pulsed field ablation prevents chronic atrial fibrotic changes and restrictive mechanics after catheter ablation for atrial fibrillation. Europace 2021;23:1767-1776.

[14] Baena-Montes JM, O'Halloran T, Clarke C, et al. Electroporation Parameters for Human Cardiomyocyte Ablation In Vitro. J Cardiovasc Dev Dis 2022;9:240.

[15] Prado LN, Goulart JT, Zoccoler M, et al. Ventricular myocyte injury by high-intensity electric field: Effect of pulse duration. Gen Physiol Biophys 2016;35:121-130.

[16] Rubinsky J, Onik G, Mikus P, et al. Optimal Parameters for the Destruction of Prostate Cancer Using Irreversible Electroporation. J Urol 2008;180:2668-2674.

[17] Jiang S, Shi H, Wang Z, et al. A Bipolar Modular Multilevel Generator Based on Half-Bridge and Special Full-Bridge for Electroporation Applications. IEEE Trans Plasma Sci 2021;49:1920-1927.

[18] Miklovic T, Latouche EL, DeWitt MR, et al. A Comprehensive Characterization of Parameters Affecting High-Frequency Irreversible Electroporation Lesions. Ann Biomed Eng 2017;45:2524-2534.

[19] Zhao Y, Yao C, Mi Y, et al. Experimental study on the killing effect of the irreversible electroporation in different frequencies. 2015 IEEE Pulsed Power Conference (PPC) 2015;1-4.

[20] Martinsen OG, Heiskanen A. Bioimpedance and bioelectricity basics. United Kingdom. Elsevier, 2023.

[21] Azura NW, Iqbal S, Taib S. LLC resonant DC-DC converter for high voltage applications. 2014 IEEE Conference on Energy Conversion (CENCON) 2014;90-95.

[22] Yao C, Zhang X, Guo F, et al. FPGA-Controlled All-Solid-State Nanosecond Pulse Generator for Biological Applications. IEEE Trans Plasma Sci 2012;40:2366-2372.

[23] Pirc E, Miklavcic D, Uršič K, et al. High-Frequency and High-Voltage Asymmetric Bipolar Pulse Generator for Electroporation Based Technologies and Therapies. Electronics 2021;10:1203.

[24] Pulsed Field Ablation (PFA) Evidence. Available at: https://www.jnjmedtech.com/en-US/service/pulsed-field-ablation-evidence

[25] Yavin H, Brem E, Zilberman I, et al. Circular Multielectrode Pulsed Field Ablation Catheter Lasso Pulsed Field Ablation: Lesion Characteristics, Durability, and Effect on Neighboring Structures. Circ Arrhythm Electrophysiol 2021;14:e009229.

[26] Medtronic completes enrollment in pivotal trial evaluating first-of-its-kind pulsed field ablation catheter for patients with atrial fibrillation Available at: https://news.medtronic.com/2022-12-05-Medtronic-completes-enrollment-in-pivotal-trial-evaluating-first-of-its-kind-pulsed-field-ablation-catheter-for-patients-with-atrial-fibrillation

[27] Reddy VY, Anter E, Rackauskas G, et al. Lattice-Tip Focal Ablation Catheter That Toggles Between Radiofrequency and Pulsed Field Energy to Treat Atrial Fibrillation: A First-in-Human Trial. Circ Arrhythm Electrophysiol 2020;13:e008718.

[28] PulseSelect™ pulsed field ablation system. Available at: https://www.medtronic.com/us-en/healthcare-professionals/products/cardiac-rhythm/ablation-atrial-fibrillation/pulseselect-pulsed-field-ablation-system.html

[29] Stewart MT, Haines DE, Verma A, et al. Intracardiac pulsed field ablation: Proof of feasibility in a chronic porcine model. Heart Rhythm 2019;16:754-764.

[30] Verma A, Boersma L, Haines DE, et al. First-in-human experience and acute procedural outcomes using a novel pulsed field ablation system: the PULSED AF pilot trial. Circ Arrhythm Electrophysiol 2022;15:e010168.

[31] FARAPULSE™ Pulsed Field Ablation System. Available at: https://www.bostonscientific.com/en-EU/products/catheters-ablation/farapulse.html

[32] Reddy VY, Dukkipati SR, Neuzil P, et al. Pulsed Field Ablation of Paroxysmal Atrial Fibrillation: 1-Year Outcomes of IMPULSE, PEFCAT, and PEFCAT II. JACC Clin Electrophysiol 2021;7:614-627.

[33] Reddy VY, Neuzil P, Koruth JS, et al. Pulsed Field Ablation for Pulmonary Vein Isolation in Atrial Fibrillation. J Am Coll Cardiol 2019;74:315-326.

[34] Reddy VY, Koruth J, Jais P, et al. Ablation of Atrial Fibrillation With Pulsed Electric Fields: An Ultra-Rapid, Tissue-Selective Modality for Cardiac Ablation. JACC Clin Electrophysiol 2018;4:987-995.

Progress in Medical Devices
eISSN: 2957-5478

Review Article https://doi.org/10.61189/871852usmbep

# Applications of vibration sensors in medicine: Enhancing healthcare through innovative monitoring

Zine Ghemari

Electrical Engineering Department, Mohamed Boudiaf University of M'sila, 28000, Algeria

**Corresponding author:** Zine Ghemari.

**Declaration of conflict of interest:** None.

Received February 11, 2024; Accepted May 6, 2024; Published June 30, 2024

## Highlights

- The article provides an overview of vibration sensors and their use in medical applications.
- Vibration sensors are used to monitor human movement, such as gait analysis and they can provide valuable data for assessing mobility, balance, and detecting abnormalities in movement patterns.
- The article explores how vibration sensors are integrated into wearable health devices, and these devices can monitor vital signs such as heart rate, respiratory rate, and sleep quality, providing continuous health monitoring.

## Abstract

Recently, vibration sensors, initially confined to industrial use, have emerged as pivotal tools in medical practice. This article delves into their myriad applications within healthcare, underscoring their potential to reshape patient care paradigms. From wearable gadgets to cutting-edge medical equipment, the incorporation of vibration sensors holds promises to redefine patient monitoring, diagnostics, and therapeutic strategies. By integrating these sensors, healthcare professionals gain novel insights into physiological dynamics, ultimately improving patient outcomes. The integration of vibration sensors into medical practice not only enhances the accuracy and efficiency of health monitoring and diagnostics but also opens up new avenues for personalized medicine. As these technologies continue to evolve, they hold the promise of transforming healthcare delivery, making it more responsive, proactive, and patient-centric.

**Keywords**: Sensor, medical, therapeutic, diagnostics, application

## Introduction

The incorporation of vibration sensors into medical devices represents a profound advancement in healthcare technology, ushering in a new era of innovation and capabilities [1]. Traditionally, vibration sensors have been primarily used in industrial applications, where they are utilized for detecting machinery faults and assessing structural integrity [2, 3]. However, the integration of these sensors into the healthcare domain signifies a significant shift from their conventional usage. This transformation marks a transformation in the pattern of technology application in medical field, opening up new avenues for improving patient care and advancing diagnostic capabilities [4-6].

One of the most notable developments in the utilization of vibration sensors in healthcare is their role in real-time monitoring and interpretation of physiological signals [7]. Previously, vibration sensors were confined to detecting mechanical vibrations in machinery, and now they are capable of capturing and analyzing subtle vibrations generated by physiological processes within the human body. These sensors can detect and measure a wide range of physiological events, including heartbeats, muscle contractions, respiratory movements, and even micro-movements associated with neurological activity [7].

The innovative applications of vibration sensors in healthcare are multifaceted and diverse. Wearable devices equipped with vibration sensors have emerged as powerful tools for the continuous, real-time monitoring of vital signs and physiological parameters [8-10]. These devices can track various metrics such as heart

**Address correspondence to: Zine Ghemari,** Electrical Engineering Department, Mohamed Boudiaf University of M'sila, P.O. Box 166, Ichbilya - M'Sila 28000, Algeria. E-mail: ghemari-zine@live.fr.

**Table 1. Simulation parameters used to simulate heart rate**

| Define parameters | Values |
|---|---|
| Sampling Frequency (Hz) | 100 |
| Number of samples | 1,000 |
| Simulate sensor data | |
| Baseline heart rate (beats per minute) | 75 |
| Standard deviation | 5 |
| Add noise to simulate variability | |
| Noise amplitude (μm) | 5 |

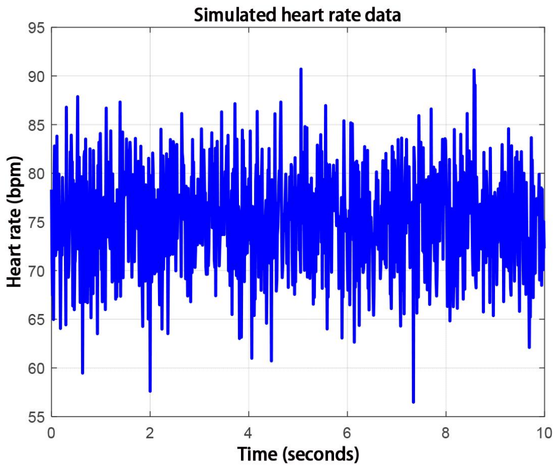


**Figure 1. Simulated heart rate.** bpm, beat per minute.

rate, respiratory rate, and activity levels, providing valuable insights into the wearer's health status and facilitating early detection of abnormalities or deviations from baseline values. Furthermore, vibration sensors can be integrated into medical implants or prosthetics to monitor their performance and functionality, ensuring optimal patient outcomes and enhancing the overall quality of care [11-13].

The integration of vibration sensors into medical devices holds immense potential for revolutionizing medical diagnostics and patient care. By enabling the collection of real-time physiological data, these sensors empower healthcare professionals with valuable information for making informed decisions and providing personalized treatment approaches [14-19]. The continuous monitoring capabilities of vibration sensors enable proactive healthcare interventions, allowing for early detection of health issues and timely interventions to prevent complications. Moreover, the data obtained from vibration sensors can be leveraged for advanced analytics and predictive modeling, facilitating the development of innovative diagnostic tools and treatment strategies [20].

This article summarizes the diverse applications of vibration sensors in healthcare, emphasizing their capacity to revolutionize patient care methodologies. From wearable devices to state-of-the-art medical apparatus, the integration of vibration sensors holds the promise of revolutionizing patient monitoring, diagnostics, and therapeutic approaches. Through the utilization of these sensors, healthcare providers stand to acquire fresh perspectives on physiological dynamics, culminating in improved patient outcomes.

**Wearable health monitoring devices**

Vibration sensors play a pivotal role in the development of wearable health monitoring devices. These sensors, when integrated into wearable gadgets, can capture subtle vibrations associated with physiological processes. The ability to monitor parameters such as heart rate, respiratory rate, and even muscle contractions provides a non-intrusive and continuous method for tracking health metrics [21].

Overall, the goal of creating a MATLAB program is to facilitate the development and testing of algorithms for wearable health monitoring applications. It allows researchers and developers to experiment with different data processing techniques, evaluate algorithm performance, and explore potential insights derived from sensor data.

To simulate different heart rate patterns or incorporate more sophisticated models in MATLAB, we use the parameters presented in **Table 1**, and the simulation results are shown in **Figure 1**.

**Figure 1** provides a visual representation of simulated heart rate measurements, aiding in the interpretation and analysis of cardiovascular activity. The horizontal axis typically represents time. Each point or interval along the axis corresponds to a specific period, such as seconds, minutes, or hours. The vertical axis indicates heart rate values. It measures the frequency of heartbeats per unit of time, usually expressed in beats per minute or another appropriate unit. The line or plot in the graph represents the simulated heart rate data. Each point on the plot corresponds to a heart rate measurement recorded at a specific time. The pattern of the line reflects changes in heart rate over time.

The plot can reveal trends or patterns in the

**Table 2. Simulation parameters used to simulate respiratory rate**

| Define parameters | Values |
|---|---|
| Sampling frequency (Hz) | 1 |
| Number of samples | 3,600 |
| Patient vital sign | |
| Heart rate mean (beats per minute) | 75 |
| Standard deviation | 5 |
| Respiratory rate mean (beats per minute) | 12 |
| Respiratory rate standard deviation (beats per minute) | 2 |

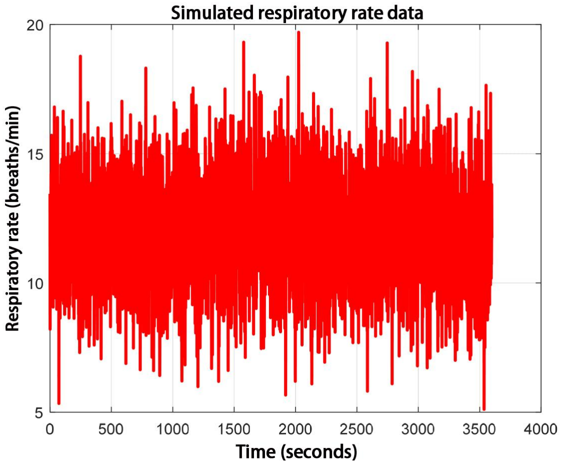


**Figure 2. Simulated respiratory rate data.**

simulated heart rate data, such as fluctuations in heart rate, periodic variations, or sudden changes indicative of physiological responses or abnormalities.

Researchers or healthcare professionals can analyze the simulated heart rate data to gain insights into cardiovascular health, monitor changes over time, or assess the effects of interventions. This analysis may involve identifying peak heart rates, calculating average heart rate values, or detecting irregularities in the heart rate pattern.

### Remote patient monitoring

In the era of telemedicine, remote patient monitoring has become increasingly prevalent. Vibration sensors enhance this practice by enabling the collection of relevant health data without physical contact. From monitoring tremors in neurodegenerative disorders to assessing respiratory patterns in chronic conditions, remote patient monitoring with vibration sensors extends the reach of healthcare services [22].

Overall, creating a MATLAB program for remote patient monitoring involves generating synthetic patient data, processing the data to extract meaningful information, and visualizing the results to facilitate interpretation and decision-making by healthcare providers. The basic example below serves as a foundational step for developing more advanced monitoring systems that can track and analyze various aspects of patient health remotely.

To simulate respiratory rate in MATLAB, we use the parameters presented in **Table 2**, and the simulation results are shown in **Figure 2**.

**Figure 2** represents a graphical depiction of simulated respiratory rate measurements over a specific period.

The line or plot in the graph represents the simulated respiratory rate data. Each point on the plot corresponds to a respiratory rate measurement recorded at a specific time. The pattern of the line reflects changes in respiratory rate over time.

### Surgical navigation and robotics

Vibration sensors find their applications in surgical navigation systems and robotics. By detecting minute vibrations during surgical procedures, these sensors provide valuable feedback to surgeons [23]. This enhanced precision is particularly beneficial in delicate surgeries, contributing to reduced invasiveness and improved postoperative outcomes [23].

Creating a surgical navigation and robotics application in MATLAB involves integrating image processing, control algorithms, and possibly hardware interfacing. **Figure 3** introduces a basic example demonstrating a simple robotic arm control system for surgical navigation.

**Figure 3** is a simulation of a straightforward 3-link robotic arm controlled to reach a target position in 3D space using a basic inverse kinematics approach. This example can be expanded by integrating more sophisticated control algorithms, implementing collision detection, incorporating real-time imaging feedback, or interfacing with actual robotic hardware for enhaced surgical precision.

### Prosthetics and orthopedics

In the realm of prosthetics and orthopedics, vi-

**Table 3. Simulation parameters used to simulate forces in prosthetic leg**

| Define parameters | Values |
|---|---|
| Acceleration due to gravity g ($m/s^2$) | 9.81 |
| Mass of the leg (kg) | 5 |
| Spring stiffness K (N/m) | 1000 |
| Time | 0:0.01:5 |

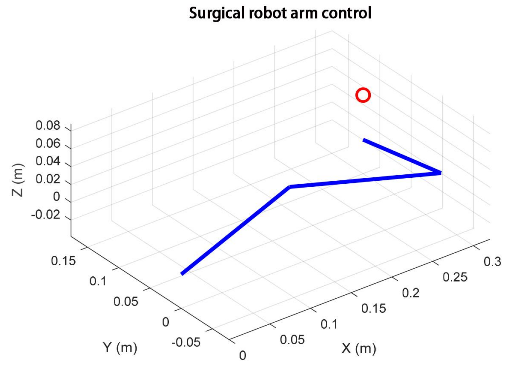


**Figure 3. Surgical robot arm control.**

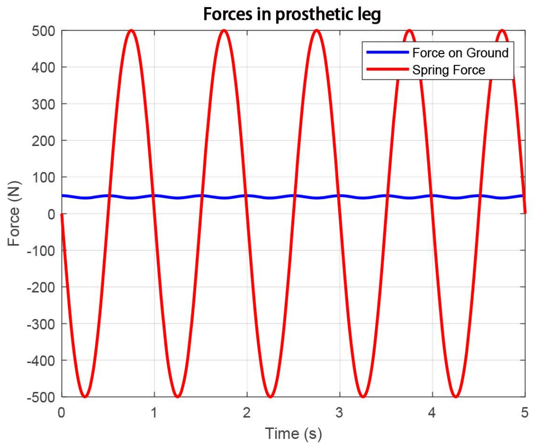


**Figure 4. Forces in prosthetic leg.**

bration sensors contribute to the development of intelligent devices. These sensors can detect changes in gait patterns, providing feedback to users and clinicians. Additionally, they play a role in monitoring the structural integrity of prosthetic limbs, ensuring optimal functionality and user satisfaction [24].

In practice, to incorporate more real-word models of leg movement and gait patterns for a more accurate simulation of walking motion. The following relationship illustrates leg angle as a function of time (simple harmonic motion):

$$\theta = \pi/6 \times \sin(2\times\pi \times t) \quad (1)$$

With:
θ: leg angle
t: time (s)

The equation below allows to calculate the force exerted by the leg on the ground:

$$F_{leg} = m_{leg} \times g \times \cos(\theta) \quad (2)$$

With:
$F_{leg}$: Force exerted by the leg (N)
$m_{leg}$: Mass of the leg (kg)

We use the following formula to calculate the force exerted by the prosthetic spring:

$$F_{spring} = -k_{spring} \times \sin(\theta) \quad (3)$$

With:
$F_{spring}$: Force exerted by the prosthetic spring
$k_{spring}$: Spring stiffness k (N/m)

Creating a MATLAB program for prosthetics and orthopedics involves various tasks such as biomechanical modeling, motion analysis, and design optimization. Below is a basic simulation result of biomechanical modeling of a simple leg prosthetic.

To simulate forces in a prosthetic leg in MATLAB, we use the parameters presented in **Table 3**, and the simulation results are presented in **Figure 4.**

**Figure 4** illustrates a specific presentation delineating the forces acting on a prosthetic leg. This visual aid is intended to complement textual discourse on forces exerted on a prosthetic leg during various activities.

Viewers or readers can interpret the information presented in the figure to gain insights into the mechanical behavior of prosthetic legs, potential challenges faced by users, and opportunities for improving design or rehabilitation strategies.

**Rehabilitation and physical therapy**

Vibration sensors are integral to rehabilitation and physical therapy practices [25]. They assist in assessing muscle activity, joint movement, and overall biomechanics during therapeutic exercises. This data-driven approach enhances the precision of rehabilitation protocols, leading to more personalized and effective treatment plans [26, 27].

The provided example in the context of MATLAB programming demonstrates a basic framework

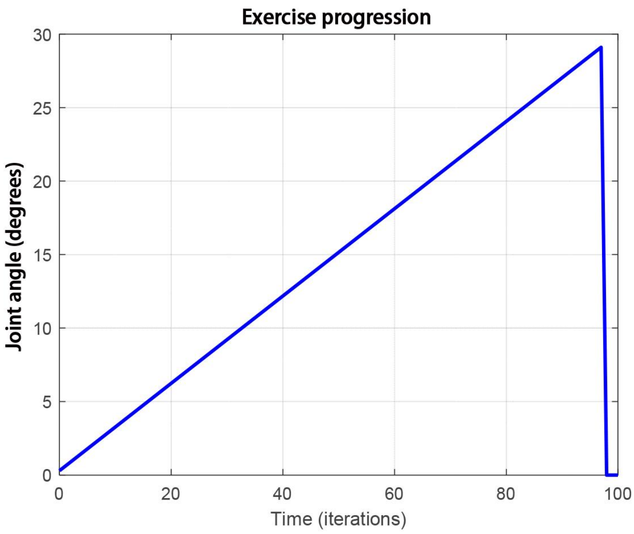


**Figure 5. Exercise progression.**

for exercise prescription and monitoring. It simulates an exercise session by gradually increasing the joint angle over time, monitoring the progression of the exercise, and visualizing the joint angle throughout the session. This basic example can serve as a foundation for developing more sophisticated rehabilitation programs using MATLAB's capabilities in biomechanical modeling, data analysis, and feedback integration (**Figure 5**).

Based on the assessment results in **Figure 5**, clear and achievable goals are established in collaboration with the individual. Goals may include improving cardiovascular health, increasing muscular strength and endurance, enhancing flexibility, weight management, injury prevention, or rehabilitation from injury or illness.

A personalized exercise program is developed to address the individual's goals, preferences, and limitations. The program typically includes a variety of exercises targeting different muscle groups and fitness components, such as cardiovascular exercise, resistance training, flexibility exercises, and neuromotor activities.

The principle of progressive overload is applied to gradually increase the intensity, duration, or complexity of exercises over time, continually challenging the body and fostering adaptation and improvement. Progression may involve adjusting resistance, repetitions, sets, exercise frequency, duration, or intensity level.

## Conclusion

In conclusion, the incorporation of vibration sensors into medical devices represents a transformative shift in healthcare technology, with extensive implications for the diagnosis, treatment, and management of various medical conditions. By harnessing the power of vibration sensors to monitor and interpret physiological signals, healthcare professionals can unlock new insights into patient health and well-being, ultimately leading to improved outcomes and enhanced quality of care. As the field continues to evolve, the innovative applications of vibration sensors are poised to drive further advancements in medical diagnostics and patient care, shaping the future of healthcare in profound and impactful ways.

**Author Contributions:** Z. Ghemari contributed to the conceptualization, methodology, original draft writing, review and editing of the manuscript, and supervision.

## Reference

[1] Bliznuks D, Cizovs J, Freimanis D, et al. Approaching Automated COPD Treatment Based on Markov Decision Process. 2023 IEEE 64th International Scientific Conference on Information Technology and Management Science of Riga Technical University (ITMS) 2023;1-5.

[2] Li C, Li J, Fang XL, et al. Application of a Method of Identifiying Instantaneous Shaft Speed from Spectrum in Aeroengine Vibration Analysis. 2022 Global Reliability and Prognostics and Health Management (PHM-Yantai) 2022;1-7.

[3] Zhao M, Shen X, Jiang F. Research on Mechanical Vibration Measurement Method Based on Event Camera. 2023 3rd International Conference on Energy Engineering and Power Systems (EEPS) 2023;528-532.

[4] S. GA, D B, Asha RM, et al. An IoT Enabled Smart Home Automation Using Augmented Reality in Computer Vision. 2023 International Conference on Self Sustainable Artificial Intelligence Systems (ICSSAS) 2023;1755-1761.

[5] Li S, Xiong Y, Zhou P, et al. mmPhone: Sound Recovery Using Millimeter-Wave Radios With Adaptive Fusion Enhanced Vibration Sensing. IEEE Trans Microwave Theory Tech 2022;70(8):4045-4055.

[6] Reguieg SK, Ghemari Z, Benslimane T. Extraction of the relative sensitivity model and improvement of the piezoelectric accelerometer performances. 2018 International Conference on Signal, Image, Vision and their Applications (SIVA) 2018;1-5.

[7] Ghemari Z, Chouaf F, Saad S. New Formula for the Piezoresistive Accelerometer Motion Acceleration and Experimental Validation. J Adv Manuf Syst 2017;16(01):57-65.

[8] Ghemari Z. Improvement of the piezoelectric sensor by the progress of the measurement accuracy. IEEE International Conference

on Smart Materials and Spectroscopy (SMS'2018) 2018.
[9] Ghemari Z, Belkhiri S. Mechanical Resonator Sensor Characteristics Development for Precise Vibratory Analysis. Sens Imaging 2021;22(1):40.
[10] Ghemari Z, Saad S. Reducing the Measurement Error to Optimize the Sensitivity of the Vibration Sensor. IEEE Sens J 2014;14(5):1527-1532.
[11] Khan NU, Ahmad S, Janjua MM, et al. The Design of Vibration Nomograph for the Vehicle Vibrations Affecting Man. 2022 Advances in Science and Engineering Technology International Conferences (ASET) 2022;1-7.
[12] Alamro H, Marzouk R, Alruwais N, et al. Modeling of Blockchain Assisted Intrusion Detection on IoT Healthcare System Using Ant Lion Optimizer With Hybrid Deep Learning. IEEE Access 2023;11:82199-82207.
[13] Ghemari Z, Belkhiri S, Saad S. Improvement of the Relative Sensitivity for Obtaining a High Performance Piezoelectric Sensor. IEEE Instrum Meas Mag 2023;26(4):49-56.
[14] Okada T, Isobe M, Kosaka T, et al. Study on Electric Motor Vibration Suppression by Active Dynamic Vibration Absorber. 2023 IEEE International Electric Machines & Drives Conference (IEMDC) 2023;1-7.
[15] Yan H, Zhang C, Wang G. Experimental Study on Dual-channel Active Control Method for Transverse Vibration of Ship Propulsion Shaft System. 2023 7th International Conference on Transportation Information and Safety (ICTIS) 2023;1353-1356.
[16] Ghemari Z. Enhancement of the vibratory analysis technique by the accelerometer characteristics evolution. The 7th International Conference on Control Engineering & Information Technology 2019.
[17] Ghemari Z, Belkhiri S, Saad S. A capacitive sensor with high measurement accuracy and low electrical energy consumption. Appl Phys 2023;129(5):362.
[18] Hao C, Xinyu D, Ling L, et al. Test and Analysis of Acoustic and Vibration Characteristics of Transformer in Winding and Iron Core Loose. 2023 IEEE 3rd International Conference on Power, Electronics and Computer Applications (ICPECA) 2023;1644-1647.
[19] Wang B, Zhang H, Cao M, et al. Parameter analysis and experimental verification of dynamic vibration absorption design for transformer tank wall. 2022 7th Asia Conference on Power and Electrical Engineering (ACPEE) 2022;830-837.
[20] Wang Y, Xia Z, Xie R. Vibration control technology of ship transmission based on machine learning. 2022 International Conference on Artificial Intelligence in Everything (AIE) 2022;580-584.
[21] Izhar M, Naqvi SAA, Ahmed A, et al. Enhancing Healthcare Efficacy Through IoT-Edge Fusion: A Novel Approach for Smart Health Monitoring and Diagnosis. IEEE Access 2023;11:136456-136467.
[22] Padmanaban K, Sarojini R, Ramalingam S, et al. LoRA-IoT based Intelligent Healthcare Device for Physically Challenged People in Hospital Application using Artificial Intelligence. 2022 4th International Conference on Circuits, Control, Communication and Computing (I4C) 2022;481-485.
[23] Raj A, Sharma S, Saluja P, et al. Seamless Live Ambulance Booking System with Patient Health Monitoring: Enhancing Emergency Care. 2023 International Conference on Electrical, Electronics, Communication and Computers (ELEXCOM) 2023;1-6.
[24] Gupta M, Shamsher S, Thirumalaisamy M, et al. Real time interaction-based Healthcare monitoring during Medical Emergencies with Internet of Things. 2022 2nd International Conference on Advance Computing and Innovative Technologies in Engineering (ICACITE) 2022;915-923.
[25] Azmin A, Abdullah S, Rahiman W. Parametric Assessment of Communication Protocol for Evaluating the Efficacy of Real-Time Healthcare Data Transmission System. 2023 IEEE 13th International Conference on Control System, Computing and Engineering (ICCSCE) 2023;62-67.
[26] Zaydi H, Bakkoury Z. 4-Lead ECG Monitoring for Cardiac Care: Advancing Healthcare with Innovative Use of Connected Watches. 2023 3rd International Conference on Electrical, Computer, Communications and Mechatronics Engineering (ICECCME) 2023;1-6.
[27] Ezhilarasi M, Kumar A, Shanmugapriya M, et al. Integrated Healthcare Monitoring System using Wireless Body Area Networks and Internet of Things. 2023 4th International Conference on Innovative Trends in Information Technology (ICITIIT) 2023;1-5.